Received: 10 September 2021 | Revised: 6 January 2022 | Accepted: 24 January 2022

DOI: 10.1002/dep2.182

The Depositional Record Open Access
A journal of the International Association of Sedimentologists
WILEY

ORIGINAL ARTICLE

Multi-elemental chemostratigraphy of Triassic mudstones in eastern Svalbard: Implications for source rock formation in front of the World's largest delta plain

Fredrik Wesenlund[1] | **Sten-Andreas Grundvåg**[1] | **Victoria Sjøholt Engelschiøn**[2] | **Olaf Thießen**[3] | **Jon Halvard Pedersen**[4]

[1]Department of Geosciences, UiT The Arctic University of Norway, Tromsø, Norway

[2]The Natural History Museum, University of Oslo, Oslo, Norway

[3]Equinor ASA, Harstad, Norway

[4]Lundin Energy Norway, Lysaker, Norway

Correspondence
Fredrik Wesenlund, Department of Geosciences, UiT The Arctic University of Norway, Norway.
Email: fredrik.wesenlund@uit.no

Funding information
Norges Forskningsråd, Grant/Award Number: 228107

Abstract

The Triassic Boreal Ocean was a shallow epicontinental basin and the sink of the World's largest delta plain known to date. Nutrient and freshwater supply from this delta have been regarded as important causes for high productivity and water mass stratification, forming Middle Triassic oil-prone source rocks. Recent studies attribute upwelling and a productivity-induced oxygen minimum zone as important factors. A multi-elemental chemostratigraphic study of a Spathian–Carnian mudstone succession exposed in eastern Svalbard was performed to investigate their formation. This includes 89 samples from three localities, from which 34 elements were acquired using combustion and X-ray fluorescence analyses. The goal is to provide a correlation framework and infer the role of productivity, redox and water mass restriction on organic matter accumulation and source rock formation. These processes had major impact on the source potential. The Spathian Vendomdalen Member suggests deposition during intermittent benthic euxinia and low productivity, corresponding with a reported deep thermocline that obstructed upwelling. The lower Anisian lower–middle Muen Member shows negligible enrichment in redox-sensitive elements but *in situ* phosphate nodules, consistent with developing upwelling and moderate productivity. The middle Anisian upper Muen Member formed during high productivity and phosphogenesis and is linked with basin-wide upwelling. Productivity, phosphate and redox proxies are all strongly enriched in the upper Anisian–Ladinian Blanknuten Member. In the south-western Barents Sea, the pro-deltaic environment of the emerging Triassic Boreal Ocean delta system had terminated these conditions. The upper Ladinian upper Blanknuten Member formed within intermittent euxinic bottom waters due to the shallowing sea level. The Carnian Tschermakfjellet Formation marks the dominance of the prograding delta system and the end of Triassic oil-prone source rock formation in Svalbard.

KEYWORDS
Barents Sea, elemental chemostratigraphy, source rocks, Triassic black shales

1 | INTRODUCTION

To identify organic-rich mudstones with source rock potential and elucidate their constituent organic facies types is a principal task in any petroleum system analysis (Magoon & Dow, 1994). The depositional environment is considered a primary control on organic facies type and abundance, and thus ultimately influences the organic composition of source rocks and their resulting generation potential (England & Mackenzie, 1989; Tissot & Welte, 1984; Tyson, 1995). Elevated primary productivity (Pedersen & Calvert, 1990), oxygen depletion and organic matter (OM) preservation (Demaison & Moore, 1980) and sedimentation rate affecting OM concentration by dilution or condensation (Creaney & Passey, 1993) are considered the most influential on OM accumulation and source rock formation (Bohacs et al., 2005; Katz, 2005). These processes form complex feedback loops, and it is challenging to determine if oxygen deficiency was caused by intense primary productivity demanding the available oxygen in the water mass, or whether the physiographic conditions in the basin resulted in water mass restriction and limited bottom water oxygenation (Katz, 2005).

Marine mudstones are commonly enriched in elements that change oxidation state and solubility depending on the benthic palaeoredox conditions (Calvert & Pedersen, 2007; Jones & Manning, 1994; Morford & Emerson, 1999; Tribovillard et al., 2006). Some elements may also precipitate in the sediments by decaying necromass and provide nutrients (Goldberg & Arrhenius, 1958; Schoepfer et al., 2015; Zhao et al., 2016). Marine mudstones may therefore represent element sinks that reflect palaeoredox and palaeoproductivity conditions in a basin (Ferriday & Montenari, 2016). The recognition of unique elemental assemblages and the application of elemental chemostratigraphy have proven useful to characterise mudstone successions and discern internal boundaries (Eisenberg & Harris, 1995; Qin et al., 1985). The technique has successfully been applied to investigate climate fluctuations (Grabowski et al., 2021), weathering and erosion rates (Ramirez-Montoya et al., 2021), changing palaeoredox conditions (Hammer et al., 2019), primary palaeoproductivity (Borchers et al., 2005), ancient water mass chemistry (Algeo & Maynard, 2008) and sequence stratigraphic development of fine-grained successions (LaGrange et al., 2020; Thöle et al., 2019).

The fine granularity of mudstones often hampers sedimentological characterisation in outcrops (Potter et al., 2005). Thin sections or high-quality cores provide the best opportunities to investigate mudstones and to recognise both sedimentary and organic facies variations (Percy & Pedersen, 2020; Zuchuat et al., 2020). However, mudstone successions are rarely cored during wellsite operations and source rock studies are thus commonly based on drill cuttings (Mansour et al., 2020; Rosenberg et al., 2021; Silva et al., 2017). While drilling mud contamination may pose a serious issue for organic geochemical characterisation of cuttings (Sanei et al., 2020), its influence on the elemental assemblage is generally negligible (Craigie, 2018). Elemental studies of drill cuttings have been shown to be highly useful in mapping chemostratigraphic zones (Craigie, 2015; Wright et al., 2010) and for multilateral well steering of shale plays (Hildred, 2012; Hildred et al., 2011; Zhang et al., 2019).

Elemental chemostratigraphy is not without limitations. For instance, it has been shown that Mo–TOC (total organic carbon) correlations decrease with increasing maturity (Ardakani et al., 2016). Elements originally hosted by source rocks are found in migrated oils (Lewan, 1984). Furthermore, whole-rock analysis do not separate between authigenic and detrital elements, which can cause unreliable data for assessing palaeoenvironmental processes (Xu et al., 2012). Hydrothermal sources and post-depositional dissolution resulting in remigration of trace elements should also be considered (Tribovillard et al., 2006). Consequently, elemental chemostratigraphic studies should ideally be combined with sedimentological, petrographic, biostratigraphic and organic geochemical data when available, and further

FIGURE 1 (A) Regional map of the Norwegian Barents Sea. The red rectangle marks the study area. The black circles denote fields, discoveries or localities described in the text. The red pentagon marks the Teistberget locality from which NGS SR-1 was sampled. Modified from the Norwegian Petroleum Directorate (2017). (B) Geological map showing the NW part of Edgeøya with the Blanknuten (77°59′43.1″N, 21°11′44.1″E), Skrukkefjellet W (78°09′42.1″N, 21°12′51.1″E) and Skrukkefjellet NW (78°10′10.3″N, 21°18′01.8″E) localities marked. Modified from Dallmann and Elvevold (2015). (C) Correlation panel of the Upper Permian to Lower Cretaceous succession from the Finnmark Platform in the south to eastern Svalbard in the north. Note the diachronous, lateral facies relationship between the Lower–Middle Triassic Steinkobbe Formation and Middle Triassic Botneheia Formation, younging from south to north. Modified from the Norwegian Petroleum Directorate (2017)

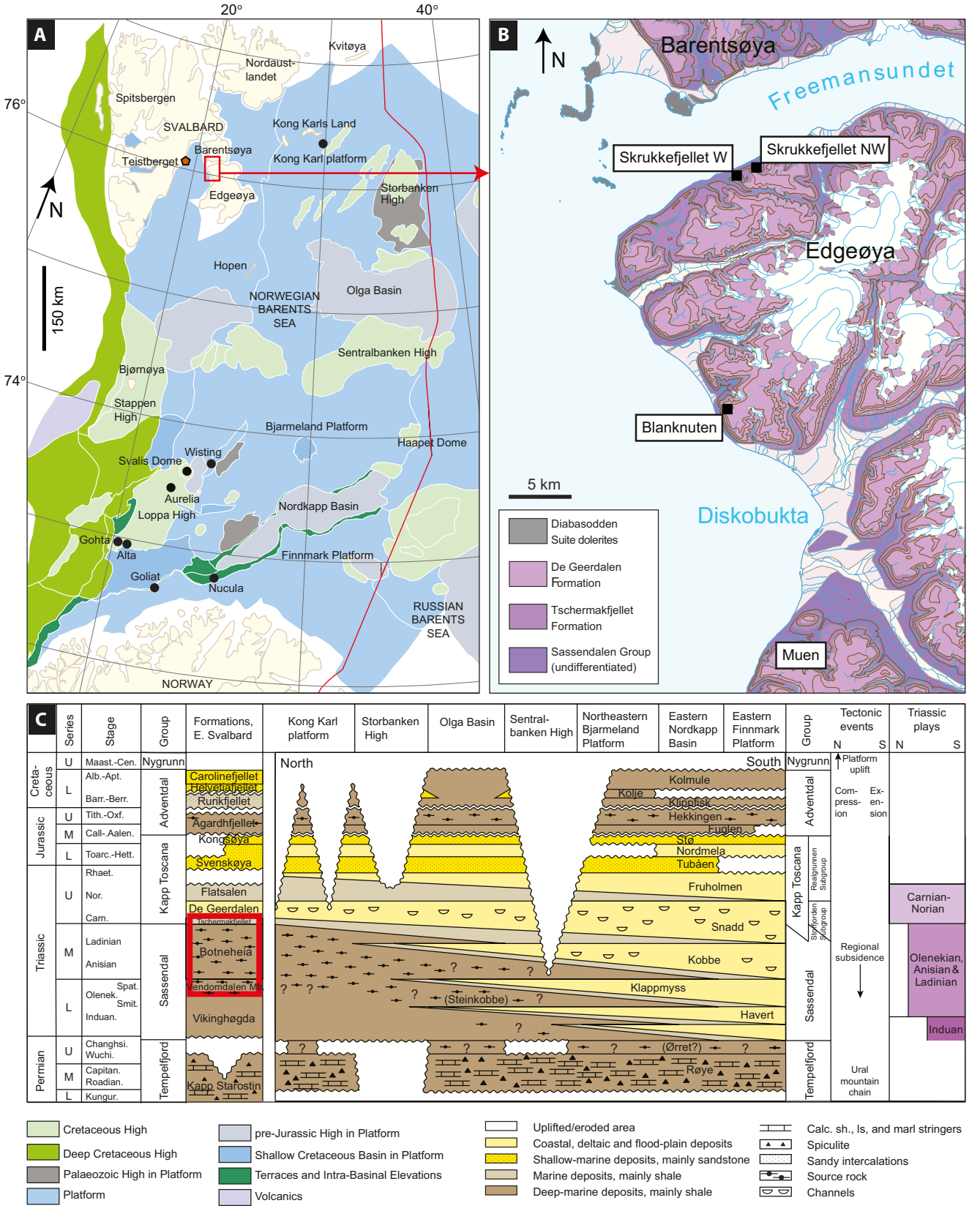

anchored to the lithostratigraphic framework of the particular study area (Craigie, 2018).

This paper presents a high-resolution, multi-elemental and multivariate chemostratigraphic study of a Triassic (Spathian–Carnian) composite mudstone succession exposed in eastern Svalbard, Arctic Norway (Figure 1). Previous studies have demonstrated that the succession has highly variable source rock potential, containing

both organic-lean, gas-prone source rocks (dominated by kerogen type III) and organic-rich, oil-prone source rocks (dominated by kerogen type II) (Abay et al., 2018; Krajewski, 2013; Lutz et al., 2021; Mørk & Bjorøy, 1984; Mørk et al., 1999). The succession includes the organic-rich mudstones of the renowned Botneheia Formation (Anisian–Ladinian), which is considered a diachronous onshore counterpart to the Steinkobbe Formation (Spathian–Anisian) in the offshore basins south of Svalbard (Lundschien et al., 2014). These genetically related and organic-rich mudstones are considered important source rock units throughout the Norwegian Barents Shelf (Abay et al., 2018; Krajewski, 2013; Lerch et al., 2016a, 2016b, 2017, 2018; Norwegian Petroleum Directorate, 2017). Collectively, these two formations accumulated in a basin floor setting in front of a large north-westward prograding delta, here termed the Triassic Boreal Ocean (TBO) delta system (Figure 2). These formations thus exhibit a diachronous relationship, younging from the south-east to the north-west across the Barents Shelf. Recent studies have suggested that the associated delta plain may have been the World's largest (Klausen et al., 2019), causing a large influx of fresh water and terrestrial OM into the marine basin (Paterson et al., 2016, 2017).

At least three models have been discussed for the depositional conditions of the Botneheia Formation. Leith et al. (1993) argue that a potential land mass termed Crockerland north of Arctic Canada (Embry, 1993) could form an enclosed basin setting that promoted benthic water mass restriction, allowing marine OM to be preserved during moderate productivity. Høy and Lundschien (2011) and Vigran et al. (2008) considered water mass stratification and high surface productivity promoted by river-supplied, nutrient-rich fresh water as the primary mechanisms for elevated OM production and anoxic–dysoxic benthic conditions. Krajewski (2008, 2013) suggested organic productivity and oxygen depletion to be a product of intense upwelling caused by favourable atmospheric circulation (Parrish & Curtis, 1982), resulting in widespread phosphogenesis and the development of an oxygen minimum zone (OMZ). Clearly, a complete understanding of the processes that controlled the fluctuating redox conditions and primary production intensities in the basin are still lacking. By integrating whole-rock X-ray fluorescence (XRF) data with TOC, total inorganic carbon (TIC) and total sulphur (TS) geochemistry, as well as sedimentological descriptions, this study provides a novel approach to investigate changes in these depositional conditions in front of the TBO delta system.

The main objectives of this paper are thus to:

1. Characterise the chemostratigraphic development of the Spathian–Carnian mudstone-dominated succession in eastern Svalbard using major, minor and trace elements.
2. Test whether the recognised chemostratigraphic units reflect the previously assigned lithostratigraphic subdivision of the succession (cf. Krajewski, 2008, 2013; Wesenlund et al., 2021).
3. Apply and compare elemental proxies to understand fluctuations in palaeoproductivity and palaeoredox conditions, variations in water mass restriction and non-biogenic vs. biogenic sedimentation and evaluate their influence on regional source rock quality, richness and distribution.

2 | GEOLOGICAL SETTING

This study focusses on a Lower–Upper Triassic organic-rich mudstone succession in eastern Svalbard and includes the Vendomdalen Member (Spathian) of the Vikinghøgda Formation (Lower Triassic), the Botneheia Formation (Anisian–Ladinian), and the lower part of the Tschermakfjellet Formation (Carnian) (Figure 1). The succession accumulated in an epicontinental embayment on the north-western margin of Pangea here referred to as the TBO (Figure 2). The embayment faced the deep Panthalassic Ocean to the north and landmasses to the east–south-east (i.e. Novaya Zemlya and the northern margin of the Baltic Shield) and to the west–north-west (i.e. Greenland) (Glørstad-Clark et al., 2010; Mørk et al., 1982; Sømme et al., 2018). The northern Barents shelf, including Svalbard, was part of a platform representing the central part of the embayment, acting as a site for mud deposition throughout major parts of the Triassic (Eide et al., 2018; Klausen et al., 2015; Riis et al., 2008). Despite the fact that there is evidence of local fault activity and structurally controlled provenance shifts (Anell et al., 2013, 2016; Gilmullina et al., 2021; Muller et al., 2019; Ogata et al., 2018), the platform was overall tectonically stable throughout the Triassic (Faleide et al., 1984; Riis et al., 2008). Following the Uralian orogeny, the south-eastern region of the Barents Shelf saw the arrival of the large, north-westward-prograding TBO delta system in Early Triassic times (Figure 2), eventually prograding across Svalbard during the Late Triassic (Glørstad-Clark et al., 2010; Klausen et al., 2019; Riis et al., 2008).

The mudstones of the Lower Triassic Vikinghøgda Formation were deposited in storm-influenced, shallow marine to shelf conditions and locally intercalate with deltaic sandstone wedges that built eastward into the basin across a gently sloping ramp (Figure 2) (Mørk et al., 1999; Wignall et al., 2016). This study pertains only to the Spathian Vendomdalen Member of this formation, which consists of dark, organic-rich silty mudstones

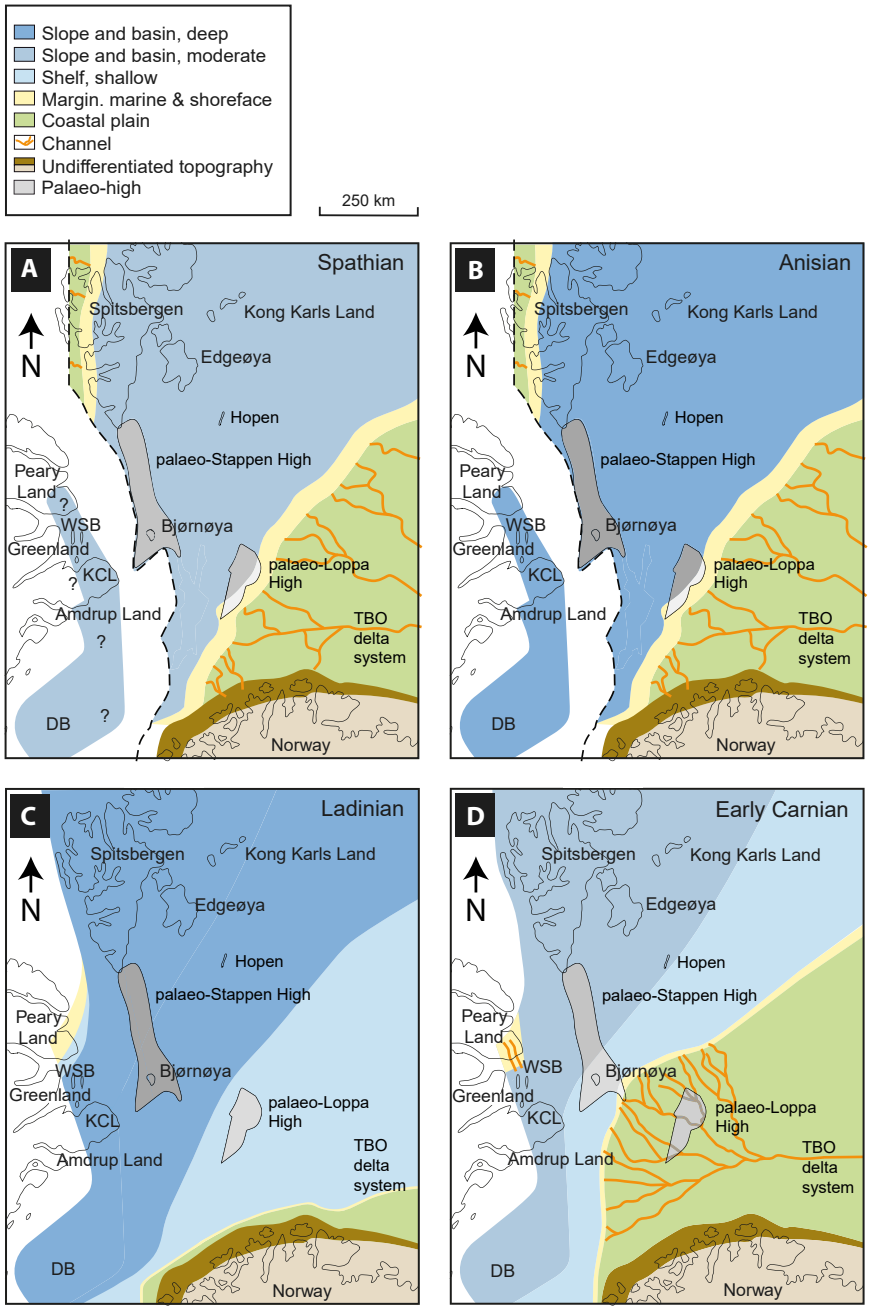

FIGURE 2 Spathian–early Carnian Triassic palaeogeography of the Barents Shelf including generalised facies distributions. DB, Danmarkshavn Basin; KCL, Kronprins Christian Land; WSB, Wandel Sea Basin; TBO, Triassic Boreal Ocean. (A) During the Spathian, eastern Svalbard was dominated by distal muds, testifying to a basinal setting and deposition of the organic-rich and silty Vendomdalen member mudstones, whereas north-eastern Greenland acted as a source area for deltaic sandstone wedges along the western basin margin. (B) The early Anisian saw shelf conditions that resulted in deposition of the lower–middle Muen Member in Svalbard. The middle–late Anisian demarcates the onset of basin-wide upwelling and phosphogenesis (not shown). (C) The Ladinian records a maximum flooding event, resulting in further deepening of the basin and widespread deposition of organic-rich mud in northern Barents Sea. In the south, pro-deltaic deposits of the Snadd Formation (Tschermakfjellet Formation facies equivalent) had reached the Svalis Dome (Figure 1A). (D) The early Carnian shows further progradation of the TBO delta system. The pro-deltaic Tschermakfjellet Formation muds of the TBO delta system eventually blanket the underlying Botneheia Formation in Svalbard. Palaeodepositional maps modified from Bjerager et al. (2019), based on Eide et al. (2018), Glørstad-Clark et al. (2010, 2011), Klausen et al. (2015), Krajewski (2013), Lundschien et al. (2014), Riis et al. (2008), Wesenlund et al. (2021)

deposited in a moderately deep and distal shelf setting below wave base (Mørk et al., 1999). The benthic conditions were suboxic to euxinic (Hammer et al., 2019; Hansen et al., 2018; Mørk et al., 1999; Vigran et al., 2014; Wignall et al., 2016; Xu et al., 2012). The Vendomdalen Member shows mainly kerogen type II/III and TOC up to

Stratigraphic unit	Locality		
	Blanknuten	Skrukkefjellet W	Skrukkefjellet NW
Vendomdalen Member	20	0	0
Lower-middle Muen Member	16	0	0
Upper Muen Member	5	0	0
Lower Blanknuten Member	7	0	1
Middle Blanknuten Member	12	0	9
Upper Blanknuten Member	6	1	5
Tschermakfjellet Formation	1	4	2
Sum:	67	5	17

TABLE 1 The investigated localities and number of samples for each stratigraphic unit. The study localities are shown in Figure 1B. See the supplementary material for the samples deriving from Wesenlund et al. (2021)

6 wt% (Bjorøy et al., 2009; Krajewski, 2013; Mørk et al., 1999). An *in situ* oil-filled hollow-chambered ammonoid (*Svalbardiceras spitzbergensis*) outcropping in this member in Central Spitsbergen proves its oil generation potential (Pedersen et al., 2020). The age-equivalent lower Steinkobbe Formation (Spathian) in the southern Barents Sea is considered the principal source rock for the Wisting discovery (Lerch et al., 2018), displaying kerogen types II and II/III with TOC up to 9 wt% in the immature shallow stratigraphic well cores in the Svalis Dome area (Abay et al., 2018; Mørk & Elvebakk, 1999).

A circum-Arctic flooding event of early Anisian age marks the base of the overlying Middle Triassic Botneheia Formation (Gilmullina et al., 2021; Mørk et al., 1989). The Botneheia Formation consists of the Muen Member (Anisian) in its lower part, and the Blanknuten Member (Anisian–Ladinian) in its upper part. The upper part of the Muen Member indicates the onset of regional phosphogenesis and abundant matrix-filled phosphatic mudstones that continue into the overlying and characteristic cliff-forming Blanknuten Member (Krajewski, 2008). These phosphate-bearing mudstones are by far the richest source rock units of the region, dominated by kerogen type II and TOC up to 12 wt% (Krajewski, 2013; Mørk & Bjorøy, 1984; Wesenlund et al., 2021). These mudstones were deposited in a deep shelf environment influenced by upwelling of nutrient-rich water from the Panthalassic Ocean during a transgressive to highstand phase (Figure 2B) (Krajewski, 2013). Fluvial runoff from the TBO delta system is also considered a significant nutrient source and driver for organic-rich shale formation (Høy & Lundschien, 2011; Vigran et al., 2008). The oil generation potential of these source rocks is shown by interbedded bitumen-stained siltstones (Schou et al., 1984), and the discovery of yet another *in situ* oil filled hollow-chambered Ladinian ammonoid (*Aristoptychites trochleaeformis*) (Smelror & Sollid, 2007).

The boundary between the Blanknuten Member (Botneheia Formation) and the overlying Tschermakfjellet Formation represents the onset of an early Carnian regional flooding event (Vigran et al., 2014). The Tschermakfjellet Formation exhibits a large-scale coarsening and shallowing upward trend and thus represents the pro-deltaic, lateral distal part of the overlying delta front to delta plain succession of the Upper Triassic De Geerdalen (Svalbard) and Snadd (Barents Sea) formations (Klausen et al., 2015; Lord et al., 2017; Mørk et al., 1982). Collectively, these units are part of the large TBO delta system that prograded from the Uralides across the Barents Shelf eventually reaching Svalbard in Late Triassic times (Klausen et al., 2019). The Tschermakfjellet Formation mudstones show dominantly gas-prone (type III) kerogen and TOC =1–3 wt% (Abay et al., 2018; Krajewski, 2013; Mørk & Bjorøy, 1984; Mueller et al., 2014).

3 | MATERIALS AND METHODS

3.1 | Field work

The Blanknuten, Skrukkefjellet W and Skrukkefjellet NW localities (Figure 1B) were previously investigated by Wesenlund et al. (2021, their figure 1b) in the coastal exposures of north-western Edgeøya and forms the basis of the lithostratigraphic logs, facies classification and sample set used in this study. In the Blanknuten locality, a *ca* 120 m thick vertical section was logged and sampled, covering the upper *ca* 40 m of the Vendomdalen

Member (Vikinghøgda Formation), the entire Botneheia Formation and the lowermost few metres of the overlying Tschermakfjellet Formation. See Table 1 for an overview of the sample set. At the Skrukkefjellet W locality, only the upper part of the Blanknuten Member (Botneheia Formation) and the lower *ca* 20 m of the Tschermakfjellet Formation were logged and sampled. At the Skrukkefjellet NW locality, the sample profile starts immediately below the base of the middle Blanknuten Member and terminates within the first few metres of the Tschermakfjellet Formation. Collectively, the three sections form a stratigraphically complete composite profile that sufficiently covers the Spathian to lower Carnian succession (i.e. the Vendomdalen Member of the Vikinghøgda Formation, the entire Botneheia Formation and the lower part of the Tschermakfjellet Formation). The lithostratigraphic units and their respective boundaries are recognised at all the investigated localities and are thus correlated with high confidence (Figure 3). At each logged section, bed thickness, lithology, sedimentary structures, fabric, trace fossils and diagenetic features (e.g. phosphate nodules) were noted. During sampling, several decimetre-deep pits were dug to acquire *in situ* rock material and minimise contamination from weathering or recent OM. Additional photographs of the investigated localities including the defined lithostratigraphic units and their boundaries are provided in Wesenlund et al. (2021).

3.2 | Sample set and preparation

Of the 89 samples included in this study, 64 samples with TOC–TIC–TS data acquired from LECO analysis were collected from Wesenlund et al. (2021). The remaining 25 samples were introduced in this study and includes the Vendomdalen Member (Vikinghøgda Formation, Blanknuten locality, 20 samples), the upper Blanknuten Member (Botneheia Formation, Skrukkefjellet W locality, one sample) and the Tschermakfjellet Formation (Skrukkefjellet W locality, four samples). These samples were subjected to LECO analysis to determine TOC, TIC and TS content using the same procedures described in Wesenlund et al. (2021). Note that the samples from the Skrukkefjellet W in Wesenlund et al. (2021) were not included in this study. A complete overview of the geochemical data introduced in this study and those obtained from Wesenlund et al. (2021) is available in Appendix S2.

Wesenlund et al. (2021) describe the following sample preparation procedures: the samples were rinsed and scrubbed in temperate, running water. Weathering skin, contemporary organic matter and/or abundant calcite veins were removed from the samples. The samples were dried at <30°C overnight. An effort was made to remove macroscopic phosphate nodules to promote comparable samples of mainly mudstone matrix composition. An agate mortar and pestle were used to crush the mudstone fragments to gravel size. Then 1 dl of the remaining gravel-sized sample material was milled using a Retsch PM 100 with agate chamber and agate milling balls set at 450 rpm for 10 min, resulting in a homogenised, fine rock powder.

3.3 | X-ray fluorescence

The X-**ray fluorescence** (XRF) analyses in this study were performed on the same pulverised and homogenised sample set originally prepared by Wesenlund et al. (2021). The pressed pellets used for the XRF analyses were prepared in the following way: 2.4 ± 0.005 g of Fluxana Cereox binder was inserted into a sample glass. Then 9.6 ± 0.005 g pulverised rock sample was added. The binder and sample were mixed and homogenised using a Heidolph Reax top vortex mixer for 2 min at 1750 rpm, later transferred and evenly distributed into a Vaneox 40 mm pressing die, then pressed at 20 t using a Vaneox 25-ton automatic press, yielding a press pellet ready for analysis.

The major, minor and trace element measurements were analysed using a Bruker S8 Tiger wavelength dispersive X-ray fluorescence (WDXRF) spectrometer in vacuum mode utilising four crystals (XS-55, PET, LiF200 and LiF220) and an OEG95LT rhodium X-ray tube. The collimator was set at 0.23°, and the sample mask diameter was 34 mm. The energy calibration for the major elements Si, Al, K, Ca, Mg, Na, P and Se was done by the standardless semi-quantitative Bruker Spectra^{plus} software (Quant Express) package using the 'best detection' method with run duration of *ca* 18 min/sample. The energy calibration for the major, minor and trace elements Sc, Ti, V, Cr, Mn, Fe, Co, Ni, Cu, Zn, Ga, As, Rb, Sr, Y, Zr, Nb, Mo, Sn, Sb, Cs, Ba, La, Ce, Pb, Th and U was done by the quantitative Bruker Spectra^{plus} software (Geo *Quant T*) package using a run time of *ca* 38 min/sample and automatic matrix correction.

To check for analytical accuracy, the Norwegian Geochemical Standard Svalbard Rock – 1 (NGS SR-1), a mudstone standard maintained by the Norwegian Petroleum Directorate (NPD) and described by Dahlgren et al. (1998), was analysed and compared with its original data sheet (Table 2). Additionally, the TOC–TIC–TS values for the NGS SR-1 used in this study were collected from Dahlgren et al. (1998). No shale standards were utilised in the XRF energy calibration. The XRF results in this study should thus be regarded as specific to the methods above and semi-quantitative. However, the analytical precision was considered good and sufficient for chemostratigraphic purposes, as TS from LECO

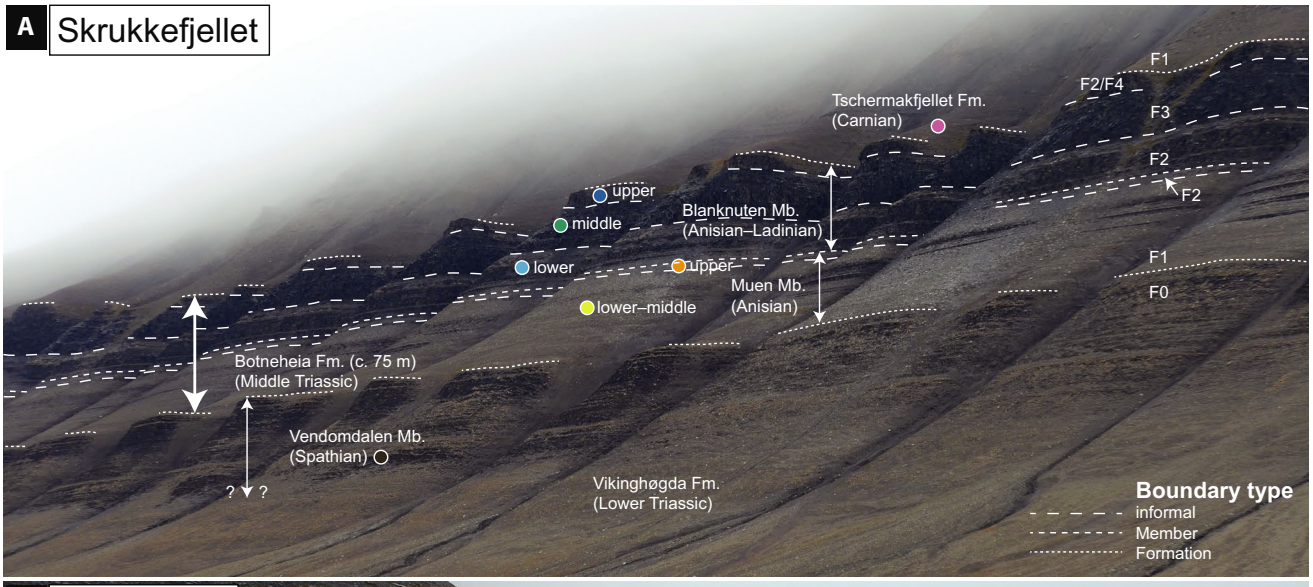
A Skrukkefjellet
F1
F2/F4
F3
F2
F2
F1
F0
Tschermakfjellet Fm.
(Carnian)
upper
middle
lower
Blanknuten Mb.
(Anisian–Ladinian)
upper
lower–middle
Muen Mb.
(Anisian)
Botneheia Fm. (c. 75 m)
(Middle Triassic)
Vendomdalen Mb.
(Spathian)
? ?
Vikinghøgda Fm.
(Lower Triassic)
Boundary type
informal
Member
Formation

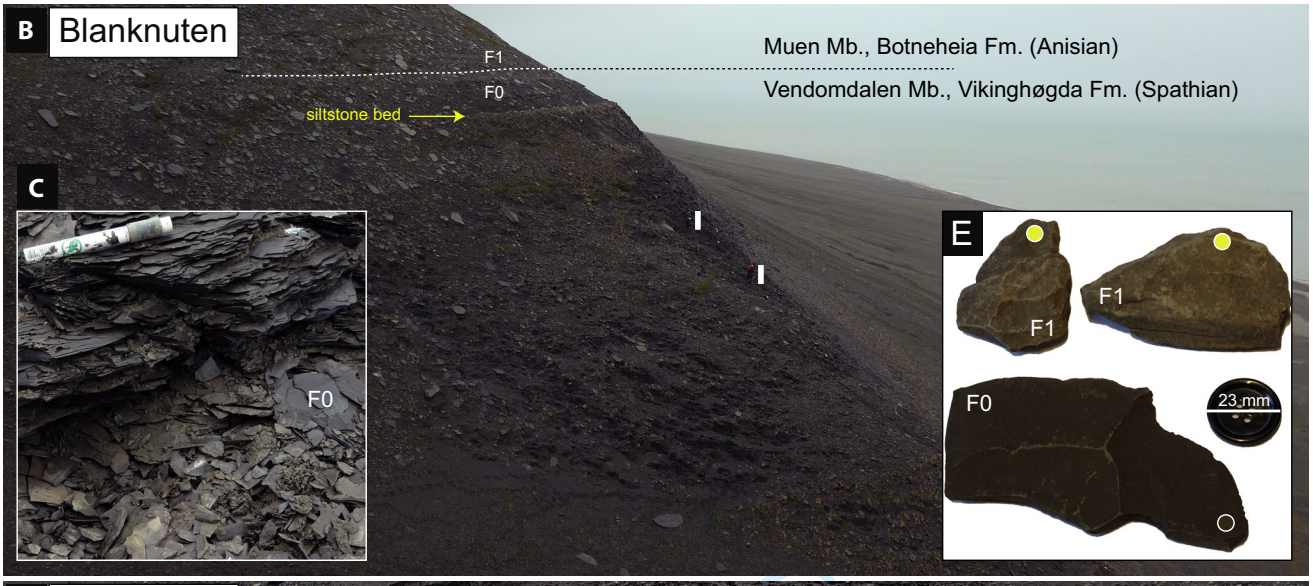
B Blanknuten
F1
F0
siltstone bed
Muen Mb., Botneheia Fm. (Anisian)
Vendomdalen Mb., Vikinghøgda Fm. (Spathian)
C
F0
E
F1
F1
F0
23 mm

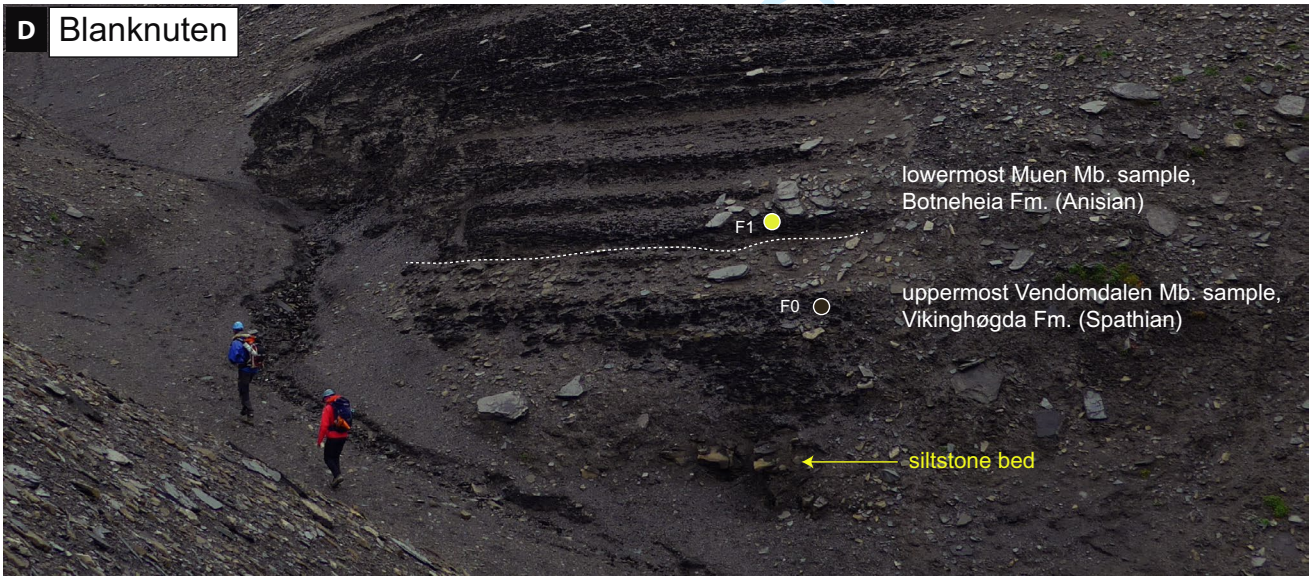
D Blanknuten
F1
F0
lowermost Muen Mb. sample,
Botneheia Fm. (Anisian)
uppermost Vendomdalen Mb. sample,
Vikinghøgda Fm. (Spathian)
siltstone bed

analysis and S from XRF analysis yielded a very strong linear correlation for the entire sample set (least squares linear regression without intercept: $S = 0.4905 \times \text{TS}$, $R^2 = 97.5\%$).

The detection of the elements Sn and Sb, both with a typical lower limit of detection = 2 ppm, was unsatisfactory and are not included in this study. Semi-quantitative determination of Se was considered unreliable; however, Se was detected in 26 of 89 samples, where 25 of these 26 samples represent the Blanknuten Member. Certain samples yielded unquantifiable U (one sample), Th (one sample), Mo (five samples) and Co (13 samples). To create a complete data matrix for multivariate analysis, the unquantified U, Th, Mo and Co values for these samples were set to 0 ppm as the lower limit of detection was typically 1–2 ppm for all these elements. Oxide–element conversions were carried out using a multiplication factor—that is the molecular weight ratio of element/oxide—for the raw data initially presented as oxides by the Spectra^{plus} software solution.

3.4 | Enrichment factors

All element enrichment factors (EFs) in this study were calculated using the following equation (Tribovillard et al., 2006): $\text{EF}_{\text{element X}} = (X_{\text{sample}}/\text{Al}_{\text{sample}})/(X_{\text{standard}}/\text{Al}_{\text{standard}})$, where 'X' is the element of interest and 'standard' is a representative reference material. In this study, the EFs for all elements except As were calculated using the post-Archean Australian shale (PAAS) (Taylor & McLennan, 1985) as the standard. The EF for As was calculated using the As value from the 'average shale' from Wedepohl (2004) and the Al value from the PAAS since As was not determined for the PAAS in Taylor and McLennan (1985). The above normalisation equation using an average shale standard is a common approach to compare elemental proxies related to depositional processes of mudstones and ideally corrects for dilution by e.g. biogenic carbonates, silica or organic carbon (Algeo & Li, 2020; Tribovillard et al., 2006). Correlations between EFs could occur due to the normalisation process itself (Van der Weijden, 2002); however, strongly correlated EFs are considered here to dominantly represent associated depositional processes (see Section 5 for discussion).

3.5 | Degree of pyritisation using total Fe

Degree of pyritisation using total Fe (DOP_T) is a palaeoredox proxy and was calculated using the following equation (Algeo & Li, 2020, their equation 2): $\text{DOP}_\text{T} = \text{TS} \times (55.85/64.12)/\text{Fe}$, where 'TS' and 'Fe' represents total sulphur from LECO analysis and total iron from XRF analysis respectively, while the coefficient 55.85/64.12 is the molecular weight ratio of Fe/TS in pyrite (FeS_2). This is opposed to distinguishing pyritic Fe and acid soluble Fe that is necessary to determine 'true' DOP (Raiswell et al., 1988). Thus, DOP_T may include minor non-pyrite sulphur and/or silicate-bound Fe, and it is necessary to calibrate DOP_T to DOP on a formation-specific basis if DOP_T is used as a proxy for DOP (Algeo & Li, 2020). However, as DOP_T and DOP correlate strongly, the variations in DOP_T still provide robust criteria to evaluate palaeoredox fluctuations (Algeo & Liu, 2020; Algeo & Maynard, 2004).

3.6 | Multivariate analysis

This study applies Pearson correlation coefficients (PCCs), PCA (principal component analysis) and HCA (hierarchical cluster analysis) for the multivariate analyses. Three samples (BLA2-18–49, BLA2-18–65 and SKØ2-18–11, see Appendix S2) were anomalously rich in TIC or P, and were discarded prior to the PCC, PCA and HCA analyses, but were otherwise included in this study. The PCC analysis, PCA and HCA preprocessing and settings were thus carried out on an 87 (samples) by 35 (variables) data matrix (including the NGS SR-1). Prior to the HCA and PCA, the parameters were rescaled in between [0,1] using min–max normalisation. The statistical analysis was performed

FIGURE 3 (A) Overview of the investigated lithostratigraphic units in outcrop view. Photograph taken from Freemansundet (see Figure 1B) looking south into the coastal exposure of the Skrukkefjellet mountain. Note the slightly more reddish hue in the Vendomdalen Member (Vikinghøgda Formation) compared to the Blanknuten Member (Botneheia Formation). The coloured circles are used to distinguish the stratigraphic units in this paper. (B) Overview of the boundary between the Vendomdalen and Muen members in the Blanknuten locality, corresponding to the VenMb–MueMb boundary in the text. Note the change in slope dip directly at the siltstone bed (yellow arrow) within the uppermost Vendomdalen Member. Two persons are highlighted with white boxes for scale. (C) Close-up photograph showing the weathering expression of the Vendomdalen Member mudstones. The marker pen is 14 cm. (D) Overview of the sample site of the uppermost Vendomdalen Member and lowermost Muen Member samples, with the VenMb–MueMb boundary marked with dashed white line. The siltstone bed is the same as the one highlighted in (B). (E) Single exposure indoor photograph of dry mudstone samples retrieved from the sample sites shown in (D). Note the distinct change in shale brightness from darker to lighter comparing the Vendomdalen Member (below) with the Muen Member (above)

TABLE 2 Comparison of major, minor and trace element concentrations of the NGS SR-1 from XRF analyses in this study and Dahlgren et al. (1998). LLD = lower limit of detection, SD = standard deviation

		NGS SR-1, this study				NGS SR-1, Dahlgren et al. (1998)					
Element	**Unit**	**Concentration**	**Stat. error (%)**	**LLD (ppm)**	**Samples**	**Min**	**Max**	**Mean**	**Median**	**SD**	**Samples**
SiO_2	%	49.67	18.30	132.7	1	53.03	54.01	53.50	53.50	0.466	5
Al_2O_3	%	13.03	0.32	133.1	1	13.91	14.30	14.07	14.00	0.180	5
CaO	%	5.17	0.31	67	1	4.60	4.92	4.80	4.82	0.123	5
K_2O	%	3.59	0.34	39.3	1	3.05	3.39	3.29	3.35	0.138	5
MgO	%	2.44	0.71	229.7	1	3.28	3.78	3.43	3.36	0.204	5
Na_2O	%	0.50	2.78	288.4	1	0.66	0.78	0.75	0.78	0.051	5
P_2O_5	%	0.18	3.48	95.6	1	0.18	0.19	0.18	0.18	0.006	5
Sc	ppm	14	9.10	2.4	1	12.8	17	14.5	14.1	1.846	4
TiO_2	%	0.78	0.29	7.9	1	0.73	0.77	0.74	0.73	0.018	5
V	ppm	533	0.31	2	1	425	647	574	588	83.221	6
Cr	ppm	62	2.36	4.4	1	80	114	89	86	12.438	6
MnO	%	0.06	1.09	7.3	1	0.06	0.06	0.06	0.06	0.002	5
Fe_2O_3	%	5.48	0.17	81.2	1	5.80	6.19	5.93	5.85	0.169	5
Co	ppm	8	1.04	1.7	1	15	20	18	18	2.136	6
Ni	ppm	77	1.63	2.5	1	68	80	73	71	4.708	6
Cu	ppm	46	2.27	2.3	1	47	57	52	51	5.033	3
Zn	ppm	139	0.79	1.7	1	146	162	152	151	5.619	6
Ga	ppm	17	1.96	0.7	1	18	19	18	18	0.812	4
As	ppm	22	16.40	2	1	14	19	17	17	3.536	2
Rb	ppm	131	0.35	0.8	1	137	154	147	148	7.028	6
Sr	ppm	113	0.37	0.7	1	112	131	119	118	6.566	6
Y	ppm	30	0.69	1	1	27	36	31	31	3.183	6
Zr	ppm	163	0.24	0.8	1	123	182	167	175	22.258	6
Nb	ppm	14	1.69	0.5	1	10	16	15	16	2.544	6
Mo	ppm	45	0.89	0.7	1	41	48	43	41	4.157	3
Ba	ppm	448	0.67	6	1	505	559	531	528	27.099	3
La	ppm	33	7.98	5.8	1	40	41	41	41	0.990	2
Ce	ppm	79	2.46	7	1	68	77	71	68	5.225	3
Pb	ppm	15	1.65	1.1	1	19	24	20	20	2.283	4
Th	ppm	6	4.51	0.9	1	11	20	15	14	4.583	3
U	ppm	5	15.10	0.9	1	8	12	9	8	2.200	4

TABLE 3 Summary of mudstone facies of non-weathered samples. F0 is from this study, while F1 to F4 are from Wesenlund et al. (2021)

Facies	Stratigraphic unit	Description	Colour	Bedding plane	Cliff-forming	Burrows	Phosphate nodules	Benthic oxygen regime	Productivity	Interpretation
F0	Vendomdalen Member	Brittle, flaky to platy mudstone	Dark brown	Smooth, straight and parallel	Yes	Not observed	Only observed in one horizon	Oxic?–euxinic	Low	Deposition from suspension fallout below wave base interrupted by rare event beds in a weakly restricted benthic setting
F1	Lower–middle Muen Member, Tschermakfjellet Formation	Soft to brittle, mostly flaky mudstone	Grey to dark grey	Smooth and rough depending on degree of bioturbation, and not always evident	No	*Chondrites* and *Helminthopsis*	Only observed in the Botneheia Formation	Oxic–dysoxic	Moderate	Deposition from suspension in a deep shelf setting interrupted by bioturbation and common event beds. More ventilated than F0 mudstones
F2	Upper Muen Member, lower and upper Blanknuten Member	Brittle and flaky to platy mudstone	Dark grey to black	Smooth, straight and parallel, but commonly deformed around phosphate nodules	Partly[a]	*Thalassinoides*	Yes, abundant	Dysoxic–anoxic	High	Deposition from suspension fallout interrupted by winnowing, bioturbation and abundant event beds. Deeper and less ventilated than F1 mudstones
F3	Middle Blanknuten Member	Brittle and platy mudstone	Black	Smooth, straight and highly parallel	Yes	Not observed	Very rare	Anoxic–euxinic	High	Deposition from suspension fallout interrupted by winnowing/reworking and rare event beds. Deeper and less ventilated than F2 mudstones
F4	Upper Blanknuten Member	Soft to brittle, platy to flaky calcareous mudstone to impure limestone	Dark grey to black	Rough, straight and parallel. Deformed around phosphate nodules	Yes	*Thalassinoides*	Yes, abundant	Dysoxic–euxinic	High	Deposition from suspension fallout interrupted by bioturbation and rare event beds. Shallower and more ventilated than F3 mudstones

[a]The upper Muen Member and lower Blanknuten Member (both F2 mudstones) are not cliff-forming and cliff-forming respectively.

using Python and the open-source scikit-learn, pandas, seaborn, numpy and matplotlib software libraries bundled with the Anaconda Data Science Platform (Anaconda, 2020). Details on script availability are given in Section 7, and the script contains all the statistical methods used in this study.

4 | RESULTS

4.1 | Facies description and stratigraphic distribution

Based on the physical appearance of the studied mudstones, Wesenlund et al. (2021) recognised and defined four dominant mudstone facies in the Botneheia Formation and the lowermost Tschermakfjellet Formation (facies F1–F4, summarised in Table 3). This study introduces a fifth facies (here referred to as F0; Table 3), restricted to the underlying Spathian Vendomdalen Member. Some of the facies are recurrent and occur in multiple stratigraphic units, whereas others are unique to specific stratigraphic units (see Table 3 and Figures 3A,B and 4). A brief facies description for F0 is given below.

Facies 0 (F0). This facies consists of cliff-forming, laminated, dark brown silty mudstones (Figures 3E and 4A) and is exclusive to the Vendomdalen Member in the upper part of the Vikinghøgda Formation. Lamination planes are smooth, straight and parallel to sub-parallel, whereas fragments are brittle and angular, and appear both flaky and platy in outcrop exposures. Burrows were not observed in the investigated section. F0 has a reddish weathering hue and exhibits clear fissility parallel to the bedding plane (Figure 3A,C). Macroscopic weathered pyrite nodules were observed. Phosphate nodules were recorded in only one horizon.

While facies transitions within mudstones may generally be difficult to discern in outcrops, the investigated succession exhibits some abrupt and clearly visible vertical facies transitions, which demarcate regional lithostratigraphic boundaries (Figure 3). The transition from the cliff-forming facies F0 (unique to the Vendomdalen Member) upwards into F1 (characterised by gentle slopes), represent the regional boundary between the Vendomdalen Member of the Vikinghøgda Formation and the lower–middle Muen Member of the Botneheia Formation (referred to as the 'VenMb-MueMb' boundary throughout this paper). In addition, the vertical transition from the cliff-forming facies F4 (unique to the upper Blanknuten Member) abruptly back to F1 marks the regional boundary between the Botneheia and Tschermakfjellet formations (referred to as the 'BlaMb-TschFm' boundary).

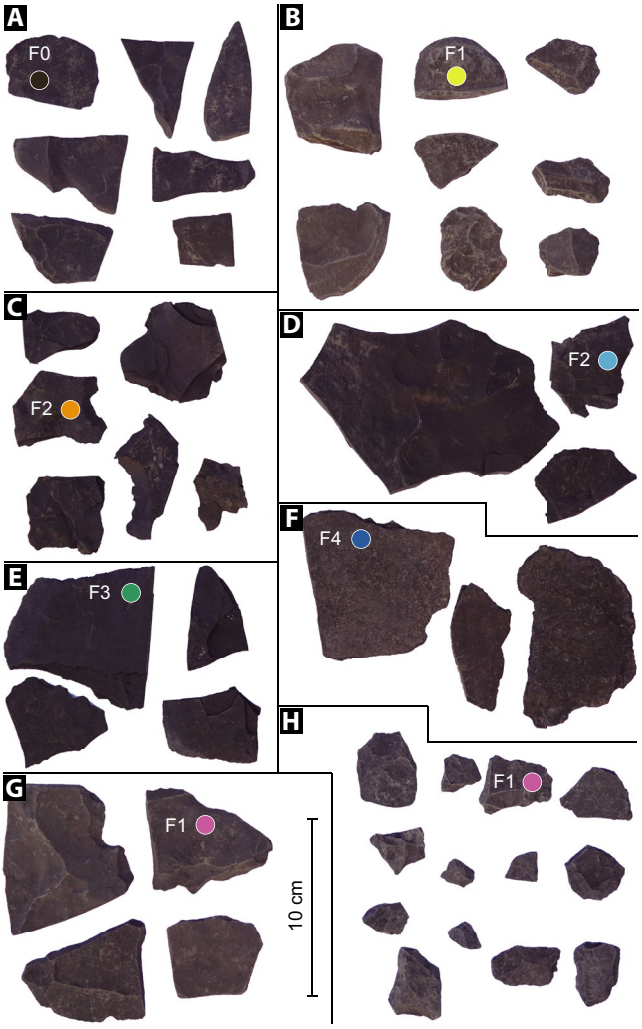

FIGURE 4 Single exposure outdoor photograph of dry mudstone fragments representing the recognised mudstone facies within the various lithostratigraphic units (characteristics summarised in Table 3). The colour-coding is the same as in Figure 3A. (A) F0, Vendomdalen Member (B) F1, lower–middle Muen Member (C) F2, upper Muen Member (D) F2, lower Blanknuten Member (E) F3, middle Blanknuten Member (F) F4, upper Blanknuten Member (G) F1, Tschermakfjellet Formation (H) F1, Tschermakfjellet Formation. Note the contrasts in brightness, clast angularity and lamination. (4A through H) and (4F) are from the Blanknuten and Skrukkefjellet W localities respectively

4.2 | Elemental chemostratigraphy

Appendix S1 shows the geochemical logs of the weight concentrations and EFs for all elements in this study, highlighting the defined facies and associated lithostratigraphic units (Figure 3, Table 3). This lithostratigraphic subdivision is supported by recent organic geochemical investigations (Wesenlund et al., 2021) and linked with the Middle Triassic informal stratigraphic units from Krajewski (2008, 2013). Appendices B and C provide the tabulated data and descriptive statistics (minimum, mean,

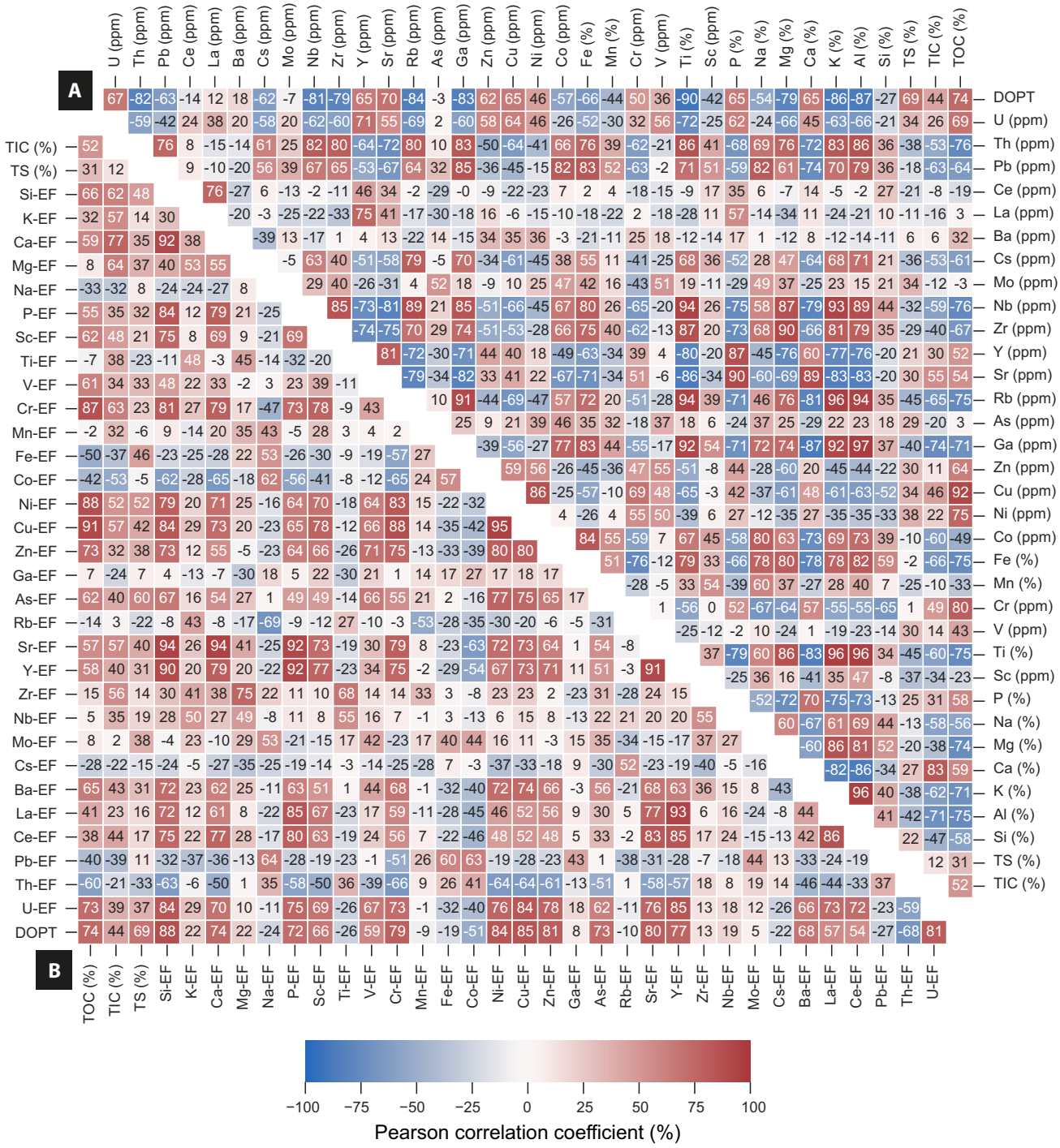

FIGURE 5 Pearson correlation coefficient (PCC) matrix, showing the linear correlation between all the variables used in this study. Three samples with anomalous TIC or P content were not included in this analysis (see Section 3.6). (A) PCCs for TOC, TIC, TS, DOP_T and element weight concentrations. (B) PCCs for TOC, TIC, TS, DOP_T and element EFs

standard deviation [SD] and maximum), respectively, for each parameter grouped by stratigraphic unit.

4.2.1 | Pearson correlation coefficient

The PCC matrix provides a full overview of the linear correlations between all weight concentrations (Figure 5A) and element EFs (Figure 5B). Aluminium (%) correlates strongly with the weight concentrations of the conservative lithogenic elements Ga, K, Ti, Rb, Zr, Nb and Th (PCC >79%, Figure 5A). Calcium, Sr, Ba, TIC and P correlate positively with each other and up to 90% PCC, but negatively with Al, indicating that Al (%) is dominantly hosted within the non-biogenic mineral fraction.

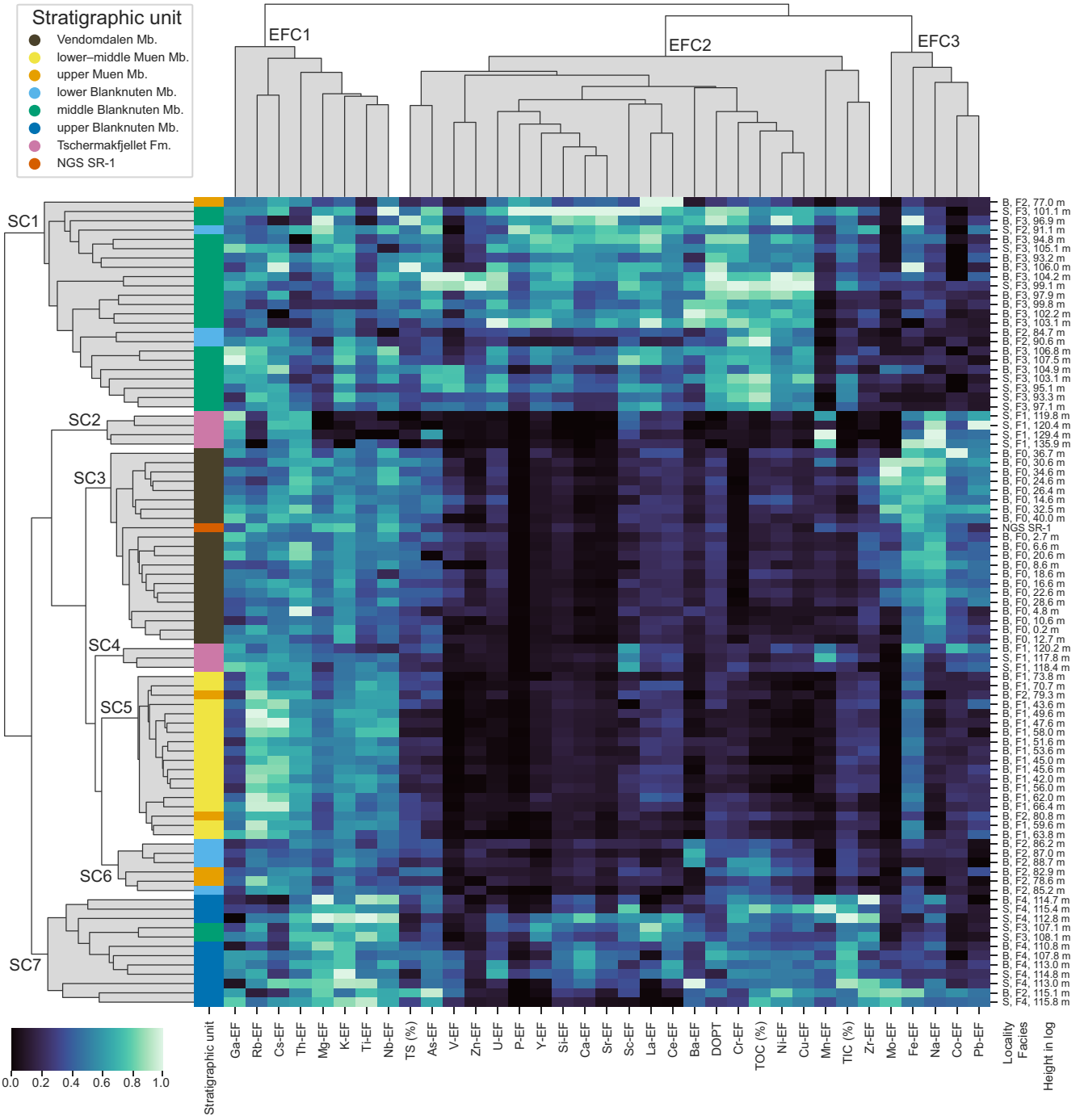

FIGURE 6 Hierarchical cluster analysis (HCA) of TOC, TIC, TS, DOP_T and element EFs. Columns and rows represent variables and observations respectively, and each column is scaled to [0,1]. The element EF clusters 1 to 3 (EFC1–EFC3) and stratigraphic clusters 1 to 7 (SC1–SC7) are described in Tables 4 and 5 respectively. Three samples with anomalous TIC or P content were not included in this analysis (see Section 3.6)

4.2.2 | Hierarchical cluster analysis

The hierarchical cluster analysis (HCA) of the TOC, TIC, TS, DOP_T and all EFs are presented in Figure 6. The analysis resulted in three main elemental EF clusters (EFCs) (Table 4) and seven main stratigraphic clusters (SCs) (Table 5). Surprisingly, The NGS SR-1 correlates best with the Vendomdalen Member and not the currently assigned Botneheia Formation.

4.2.3 | Principal component analysis

A biplot of PC1 (principal component 1) vs PC2 (principal component 2) is shown in Figure 7. PC1 and PC2 account for 59.78% of the total variance and clearly demonstrate that the assigned stratigraphic units form groups that correlate well with the stratigraphic clusters from the HCA (compare Figures 6 and 7). Likewise, EFs of Na, Mo, Fe, Pb and Co group together and are captured by the PC2, which correlates

TABLE 4 Defined enrichment factor clusters based on correlating parameters

Enrichment factor cluster	Parameters
EFC1	Ga-EF, Rb-EF, Cs-EF, Th-EF, Mg-EF, K-EF, Ti-EF and Nb-EF
EFC2	TOC, TIC, TS, DOP_T, As-EF, V-EF, Zn-EF, U-EF, P-EF, Y-EF, Si-EF, Ca-EF, Sr-EF, Sc-EF, La-EF, Ce-EF, Ba-EF, Cr-EF, Ni-EF, Cu-EF, Mn-EF and Zr-EF
EFC3	Mo-EF, Fe-EF, Na-EF, Co-EF and Pb-EF

with EFC3 (Figure 6, Table 4). Correlations between the loadings on PC1 and EFC2 are also evident (compare Figures 6 and 7). The Tschermakfjellet Formation in the PCA displays a bipartite grouping as expressed by SC2 and SC4 in the HCA (compare Figures 6 and 7). As with the HCA, the PCA shows that the NGS SR-1 correlates best with the F0 mudstones of the Vendomdalen Member (Figures 6 and 7).

The stratigraphic distribution of the PC1, PC2 and PC3 (principal component 3) scores and the loadings are shown in Figure 8. In PC1, all samples from the Vendomdalen and lower–middle Muen members show similar, negative scores. The onset of the upper Muen Member from level *ca* 75 m (Figure 8) up to the BlaMb–TschFm boundary mark a prominent positive 'bow-shaped' excursion with maximum PC1 scores in the middle Blanknuten Member. A steep, negative trend across the BlaMb–TschFm boundary results in negative PC1 scores for all Tschermakfjellet Formation samples. PC2 scores show a positive incline within the Vendomdalen Member but is abruptly terminated at the VenMb–MueMb boundary. This marks the onset of a second positive incline arguably interrupted at the BlaMb–TschFm boundary. PC3 shows a small, positive excursion across the VenMb–MueMb boundary, while the BlaMb–TschFm boundary denotes a steep negative incline and a prominent geochemical transition with positive loadings for EFs of Nb, Zr, Ti and Mg (Figure 8).

4.2.4 | Summarised chemostratigraphic log panel

A chemostratigraphic log panel including 10 features with substantial loadings on PC1, PC2 or PC3 is included (Figure 9). Chemostratigraphic logs of TS, TIC, DOP_T and the remaining element EFs and weight concentrations are available in Appendix S1. The EFs of Si, Ba and P show log trends equivalent to the PC1 log (compare Figures 8 and 9). These EFs show no enrichment in either the Spathian Vendomdalen Member (Vikinghøgda Formation, facies F0), the Anisian lower–middle Muen Member (Botneheia Formation, facies F1) or the Carnian Tschermakfjellet Formation (facies F1), but capture a 'bow trend' in the phosphogenic upper Muen and the entire Blanknuten members (Botneheia Formation) with consistently high values in its middle part (Figure 8). The TOC and Cr-EF trends are strongly coupled with each other and the variables above (Figures 5, 6, 7 and 9) but display a negative and positive excursion across the VenMb–MueMb boundary respectively. The U-EF shows strong positive loadings for PC1 and slight positive loadings for PC2 (Figure 8). In contrast, Mo-EF has the strongest loading on PC2 and a slight negative loading on PC1 (Figure 8).

The Mo-EF log clearly records the negative geochemical discontinuity at the VenMb–MueMb and BlaMb–TschFm boundaries (Figure 9) and an overall positive incline within the Botneheia Formation, consistent with the PC2 log (Figure 8). The Co-EF log resembles that of the Mo-EF, but in contrast, it shows a positive excursion across the BlaMb–TschFm boundary with equivalent values in the Vendomdalen Member (Facies F0) and Tschermakfjellet Formation (facies F1; Figure 9). The Na-EF log demonstrates a clear negative excursion directly at the VenMb–MueMb boundary and is generally constant through all the stratigraphic units in the Botneheia Formation except the upper Blanknuten Member (F2/F4 mudstones). The BlaMb–TschFm boundary marks a Na-EF reversal into the lowermost Tschermakfjellet Formation (Figure 9). Three samples in the lowermost part of this unit show an elemental assemblage comparable to the Botneheia Formation (SC4, Figure 6), contrasting its younger samples (SC2, Figure 6). These two SCs show a bipartite division in the PCA analysis (Figure 7).

The Ti-EF log records the strongest loading on PC3 (Figure 8) and shows a minor positive excursion at the VenMb–MueMb boundary and a slight negative bow shape in the Botneheia Formation with maximum values in the upper Blanknuten Member (Facies F4). A negative Ti-EF incline takes place across the BlaMb–TschFm boundary (Figure 9), as confirmed in the PC3 log (Figure 8).

5 | DISCUSSION

5.1 | Chemostratigraphic rationale

The unsupervised multivariate analyses of the elemental EFs clearly demonstrate that the various mudstone facies and their associated stratigraphic units are recognised

TABLE 5 Defined stratigraphic clusters based on recognisable criteria that separate the elemental assemblages and their sample assemblage

Stratigraphic cluster	Vendomdalen Member samples	Lower–middle Muen Member samples	Upper Muen Member samples	Lower Blanknuten Member samples	Middle Blanknuten Member samples	Upper Blanknuten Member samples	Tschermakfjellet Formation samples	Relative abundance of element EFs or EFCs
SC1	0	0	1	3	19	0	0	High EFC2 (except Mn-EF), low EFC3
SC2	0	0	0	0	0	0	4	Low EFs of Mg, K, Ti and Nb in EFC1
SC3	20	0	0	0	0	0	0	Low EFC2, high EFC3
SC4	0	0	0	0	0	0	3	Low EFC2 (except EFs of Sc and Mn), variable EFC3
SC5	0	16	2	0	0	0	0	Low EFC1 and EFC2
SC6	0	0	2	4	0	0	0	Low EFC1 and EFC3, variable EFC2
SC7	0	0	0	0	2	10	0	Variable EFC1 (but high EFs of Mg, K, Ti, Nb), variable EFC2 and EFC3 (but high TIC)

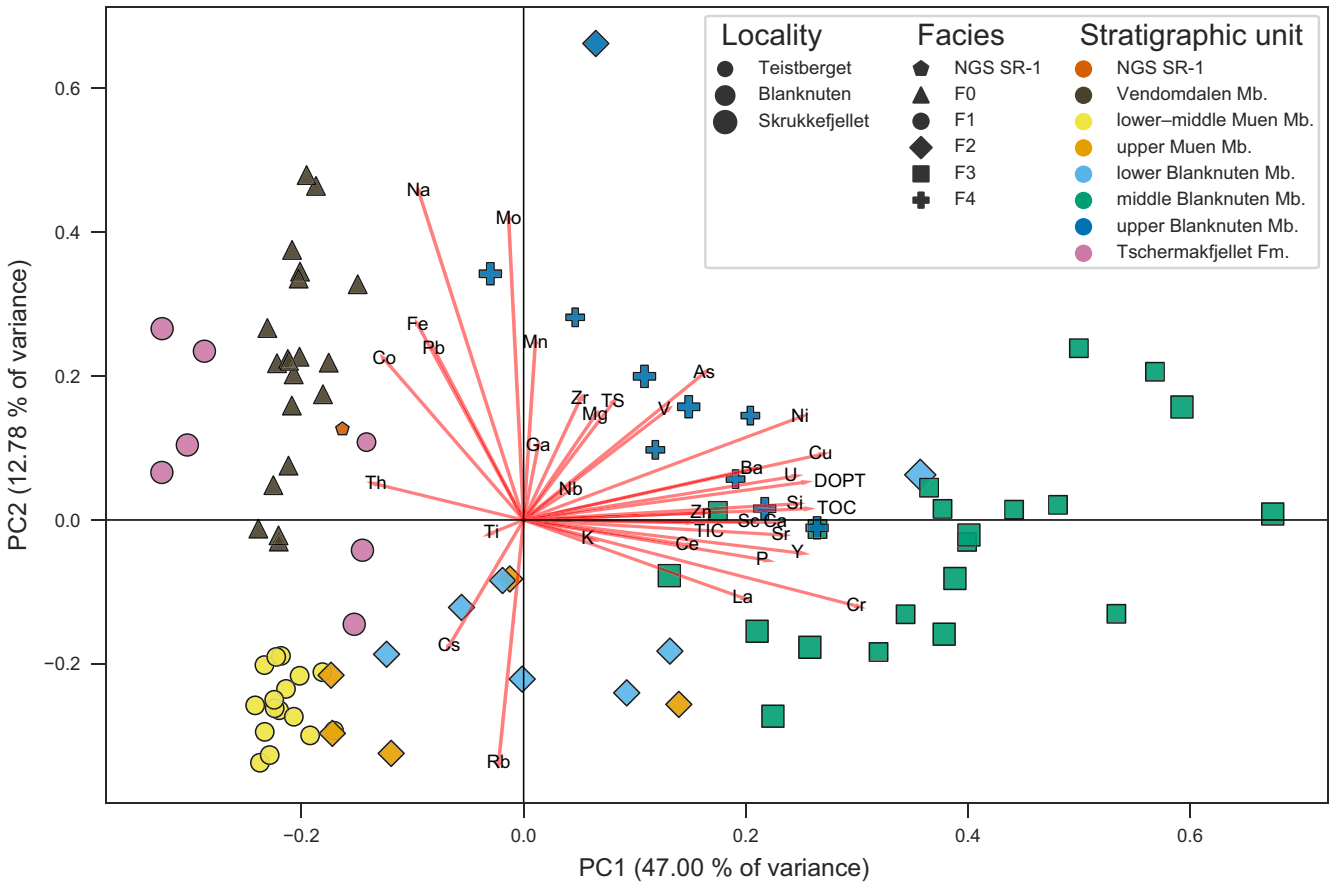

FIGURE 7 Biplot of the principal components 1 (PC1) and 2 (PC2) derived from PCA analysis of TOC, TIC, TS, DOP_T and element EFs. The axes represent the values for the loadings, while the scores are scaled by the largest range in each PC. Three samples with anomalous TIC or P content were not included in this analysis (see Section 3.6)

via distinct HCA clusters and PCA groups (Figures 6, 7 and 8). Wesenlund et al. (2021) reported that the various (informal) subunits of the Botneheia Formation (i.e. at intra-member scale) show discernable TOC, TIC, TS and bitumen variations related to facies variations and kerogen quality and richness, which further agree with previously published geochemical and Rock-Eval data (Krajewski, 2008, 2013). This indicates that the bulk of the element EFs are genetically related to inferred palaeodepositional processes that affect organic composition and hence source rock formation. Furthermore, most geochemical logs (Figure 8 and Appendix S1) clearly record the vertical facies transitions that marks the VenMb–MueMb and BlaMb–TschFm stratigraphic boundaries, demonstrating that they also represent regional geochemical boundaries. Previous studies have assigned these surfaces to the early Anisian and early Carnian flooding events, respectively, and have shown that they delimit a circum-Arctic Middle Triassic 2nd order transgressive–regressive sequence (Mørk et al., 1989). The included parameters and their excursions are therefore highly relevant as palaeoenvironmental proxies and are useful to identify regional sequence stratigraphic boundaries.

It is evident that the lower–middle Muen Member F1 and the Vendomdalen Member F0 mudstones are geochemically dissimilar (Figures 6, 7 and 8). The NGS SR-1 (Dahlgren et al., 1998), typically assigned to the Anisian Muen Member of the Botneheia Formation (Brekke et al., 2014; Lutz et al., 2021) and its strong correlation with the Spathian Vendomdalen Member F0 mudstones (Figures 6 and 7) is unfitting and must be investigated. No biostratigraphic age has been assigned to the NGS SR-1 as it was unsuitable for palynological studies (Dahlgren et al., 1998). Isolated kerogen from the NGS SR-1 shows $\delta^{13}C = -33.0‰$ (Dahlgren et al., 1998), very similar to $\delta^{13}C$ values of TOC from the upper Vendomdalen Member mudstones in central Spitsbergen (min. $\delta^{13}C = -32.9‰$) (Hammer et al., 2019, their figure 4). In both western Spitsbergen and the Sverdrup Basin, $\delta^{13}C$ of TOC from Spathian mudstones are commonly lower than Anisian mudstones and the latter are never lower than −32.0‰ (Grasby et al., 2016, 2020). It was specifically noted that phosphate nodules were not observed in the sample locality of the NGS SR-1 (Dahlgren et al., 1998). Phosphate nodules are generally absent in the Vendomdalen Member but common in the Muen

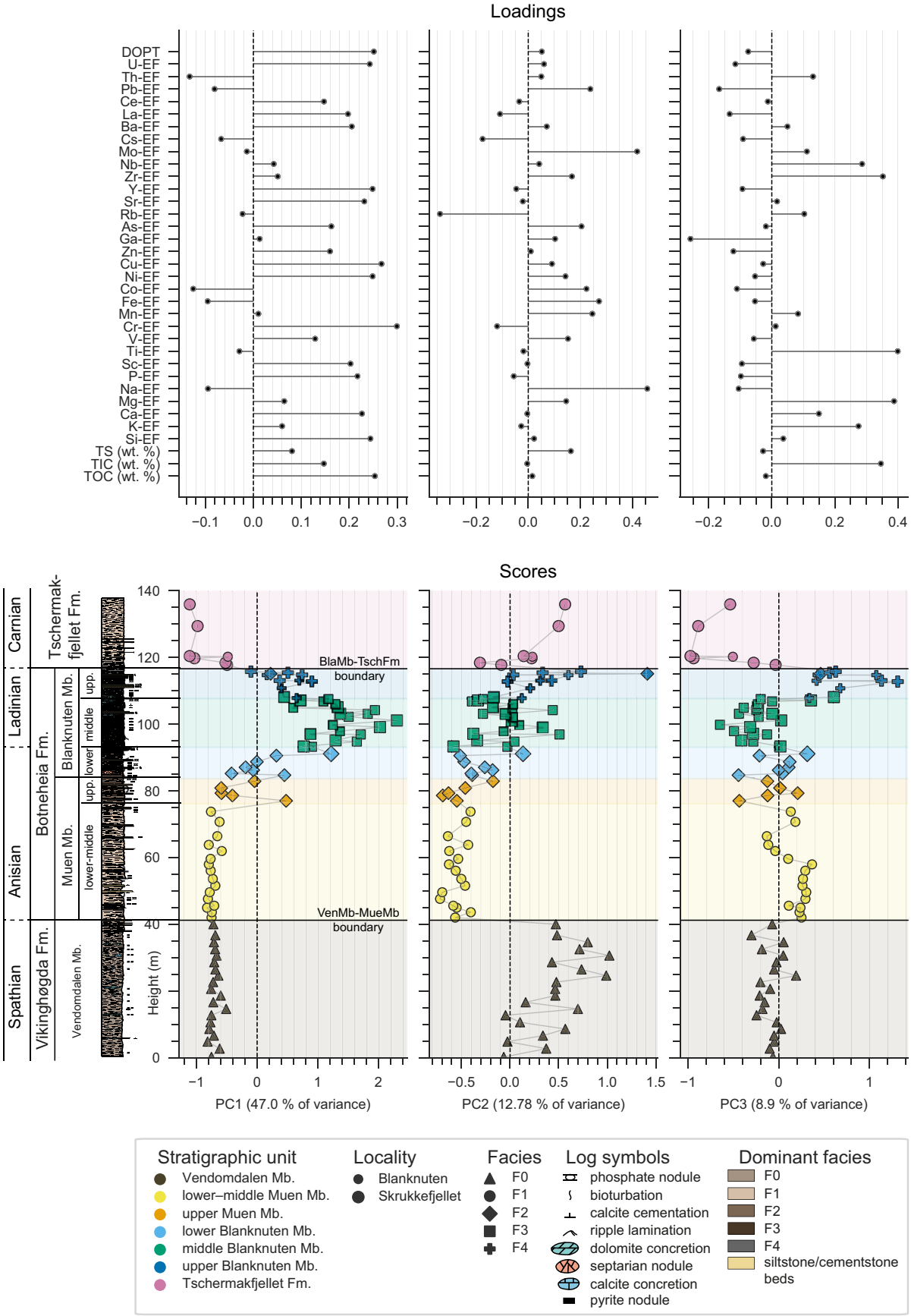

FIGURE 8 Sedimentary log and combined plots showing the PC1, PC2 and PC3 loadings on top and the corresponding stratigraphic distribution of PC1, PC2 and PC3 scores below. Note the positive bow shape in the Botneheia Formation (PC1) and the prominent discontinuities at the VenMb–MueMb boundary (PC2) and the BlaMb–TschFm boundary (PC3). Three samples with anomalous TIC or P content were not included in this analysis (see Section 3.6)

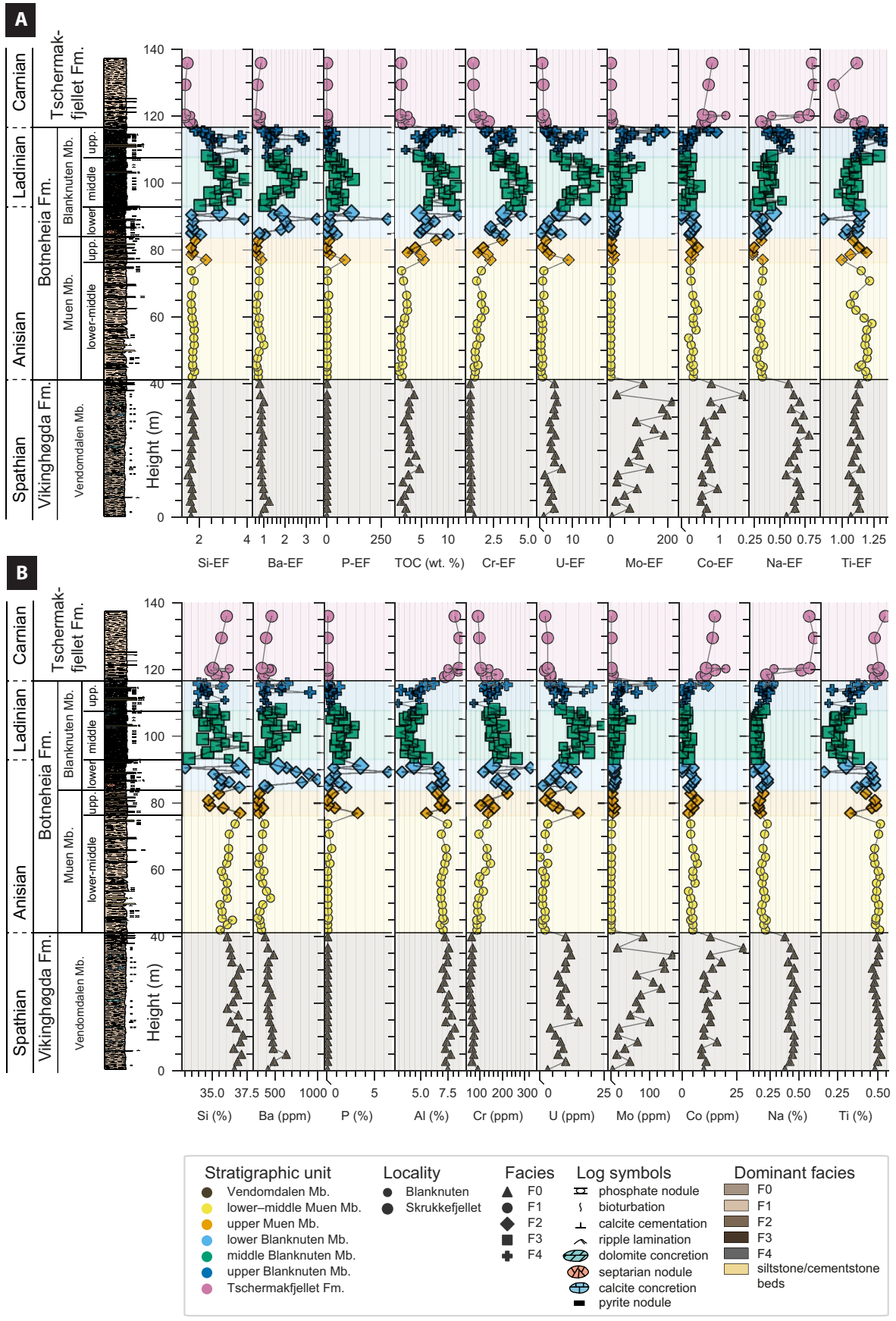

FIGURE 9 Representative log panels of selected geochemical variables with strong loadings (Figure 8), showing the geochemical development throughout the Spathian–Carnian mudstone succession. (A) TOC and element EFs. (B) Element weight concentrations

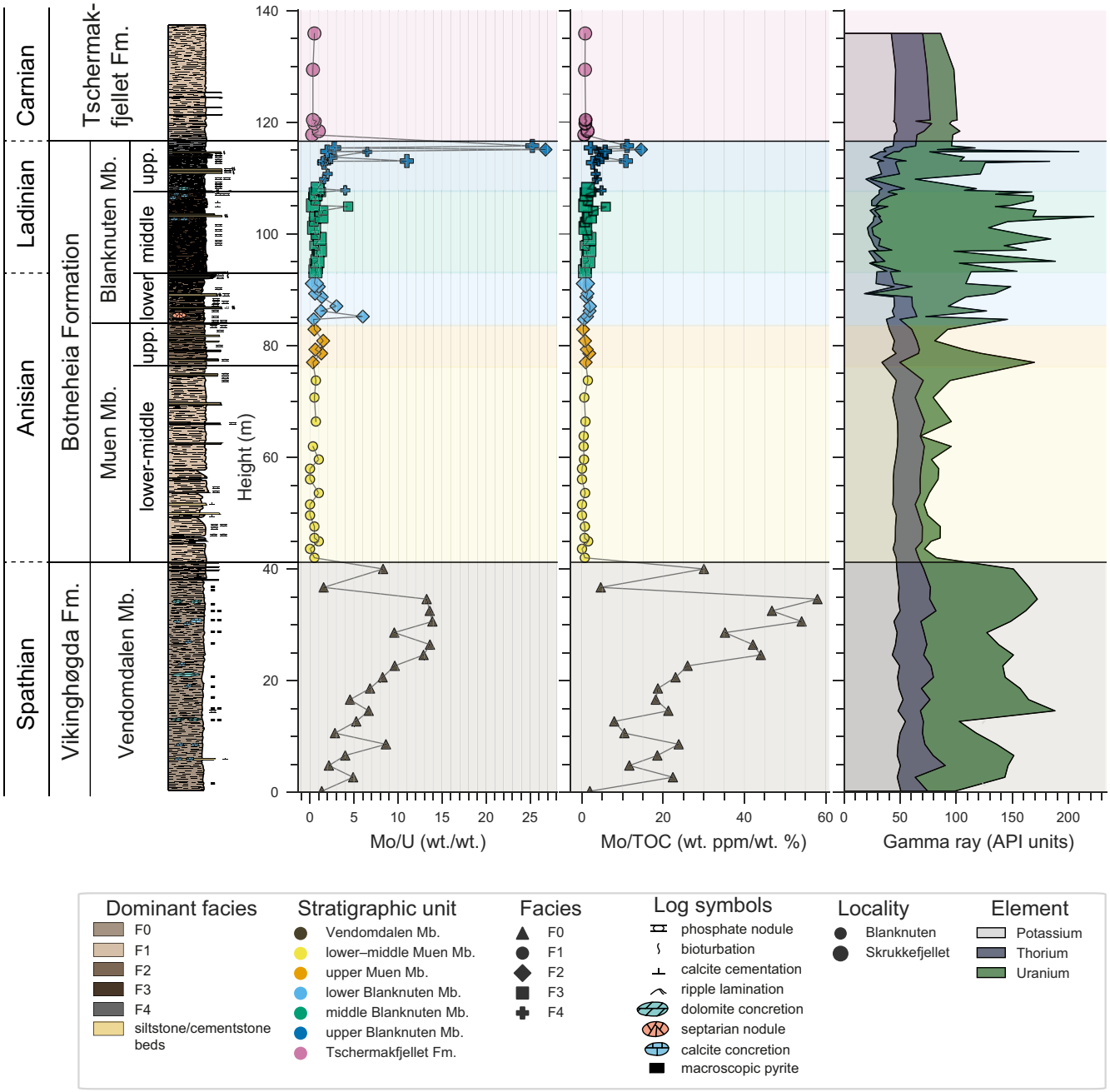

FIGURE 10 Logs of Mo/TOC, Mo/U and synthetic spectral gamma ray response calculated from K, Th and U compared with the lithostratigraphic division

Member throughout Svalbard (Vigran et al., 2014). Consequently, it is suggested that the NGS SR-1 was in fact sampled from the Vendomdalen Member, implying that cluster SC3 (which includes the NGS SR-1) only represents this stratigraphic unit (Figure 6).

5.2 | Primary productivity

The rate of primary productivity in the water column during time of deposition is a fundamental factor controlling the organic richness of mudstones (Bohacs et al., 2005; Katz, 2005). The degree of palaeoproductivity may be assessed using detrital-corrected P, Si and Ba (e.g. EFs) as proxies (Algeo et al., 2011; Eggimann et al., 1980). Biogenic carbonate enrichment is also a commonly used proxy and may be indirectly estimated using the TIC content and detrital-corrected Ca and Sr (Niebuhr, 2005; Song et al., 2014). In addition, EFs or concentrations of Cu and Ni are useful proxies for the organic matter flux or productivity, assuming sufficiently reducing conditions (Tribovillard et al., 2006). However, as Cu and Ni may also

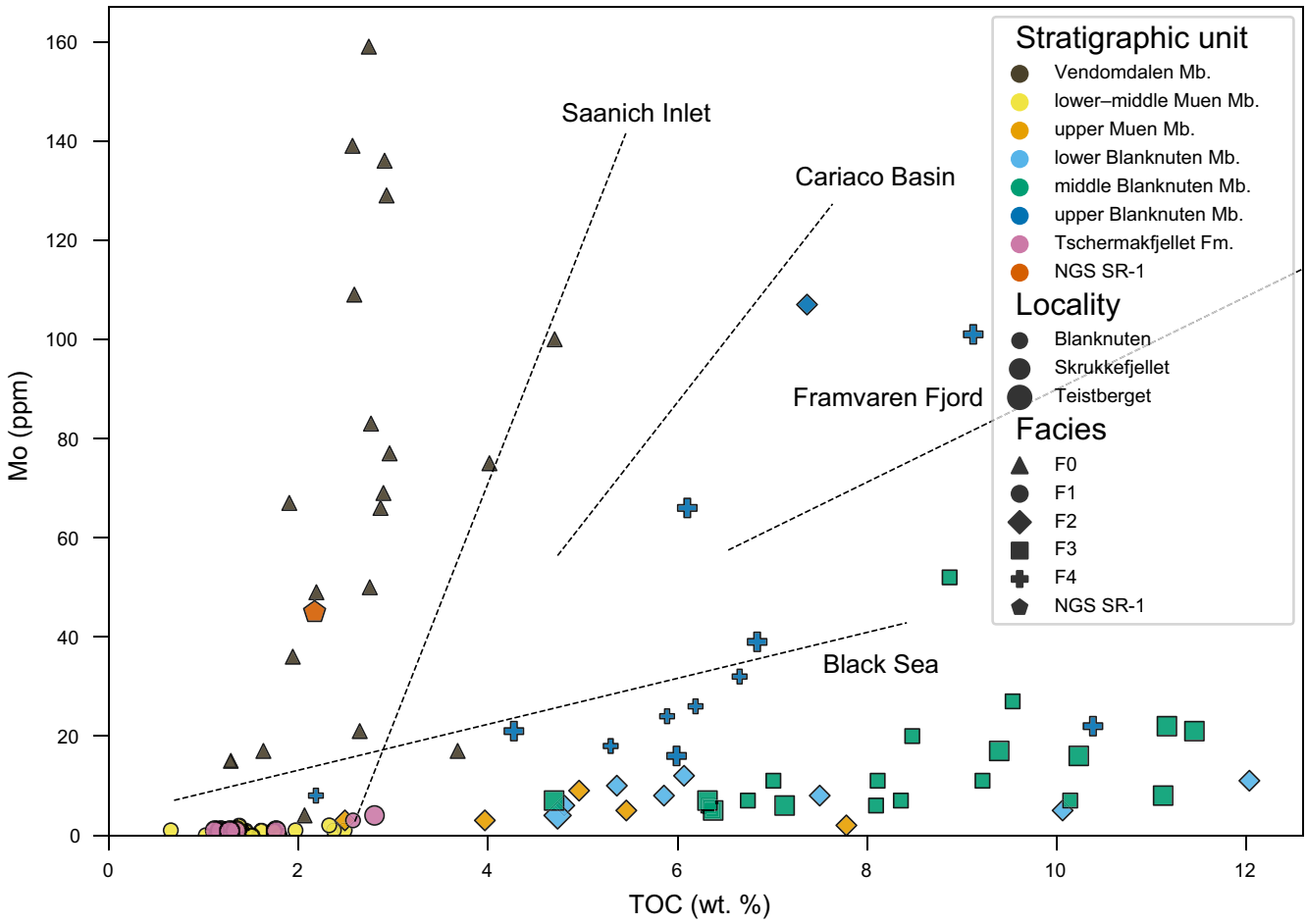

FIGURE 11 Cross plot of TOC (%) vs Mo (ppm). The dashed lines are collected from Algeo and Lyons (2006) and represent linear regression trends of TOC and Mo content in modern basins with variable water mass restriction, where the Saanich Inlet is least restricted, and the Black Sea the most restricted. The bulk data from the Blanknuten Member mudstones correlate with a Black Sea water mass restriction type but see Section 5.4 for discussion on possible misinterpretation

be concentrated in clay minerals, heavy minerals and carbonates (Craigie, 2018), their enrichment may have variable detrital influence.

The TIC content and EFs of P, Si, Ba, Ca and Sr are overall low within the Vendomdalen Member F0 mudstones (Figures 8 and 9, Appendix S1), indicating limited primary productivity in eastern Svalbard during the Spathian. A prolonged Early Triassic period with regional nutrient limitation caused by a lowered nutricline may have occurred along the northern margin of Pangea and within the TBO (Grasby et al., 2016, 2020). The depressed nutricline and limited P could be a result of high ocean temperatures caused by global hothouse conditions during the Early Triassic (Grasby et al., 2016; Sun et al., 2012).

The transition from the Vendomdalen Member F0 mudstones to the lower–middle Muen Member F1 mudstones and the associated negative geochemical excursion correspond roughly to the Spathian–Anisian boundary (Krajewski, 2008; Weitschat & Lehmann, 1983), although this formation boundary is erosional and diachronous throughout Svalbard (Hounslow et al., 2008a, 2008b). The phosphate nodules within these F1 mudstones indicate elevated primary productivity and phosphorite formation due to upwelling of nutrient-rich marine waters (Filippelli, 2011), although not sufficient to substantially increase the phosphate cement in the mudstone matrix (Figure 9) or to form an OMZ (Krajewski, 2008, 2013). This coincides with deposition during cooler, more nutrient-rich waters that initiated increased productivity during Middle Triassic times (Grasby et al., 2016, 2020). The small increase in TIC but limited Si-, P- and Ba-EFs directly above the VenMb–MueMb boundary suggest that the carbonate cement (i.e. TIC) primarily formed in concert with elevated bicarbonate alkalinity in the sediments due to increased microbial oxidation (Taylor & Macquaker, 2014).

The facies change upwards into the upper Muen/lower Blanknuten Member F2 mudstones (Figure 4) marks an abrupt increase in element EFs associated with PC1 and includes the productivity proxies TIC and EFs of Si, P, Ba, Ni and Cu (Figures 8 and 9). These F2 mudstones

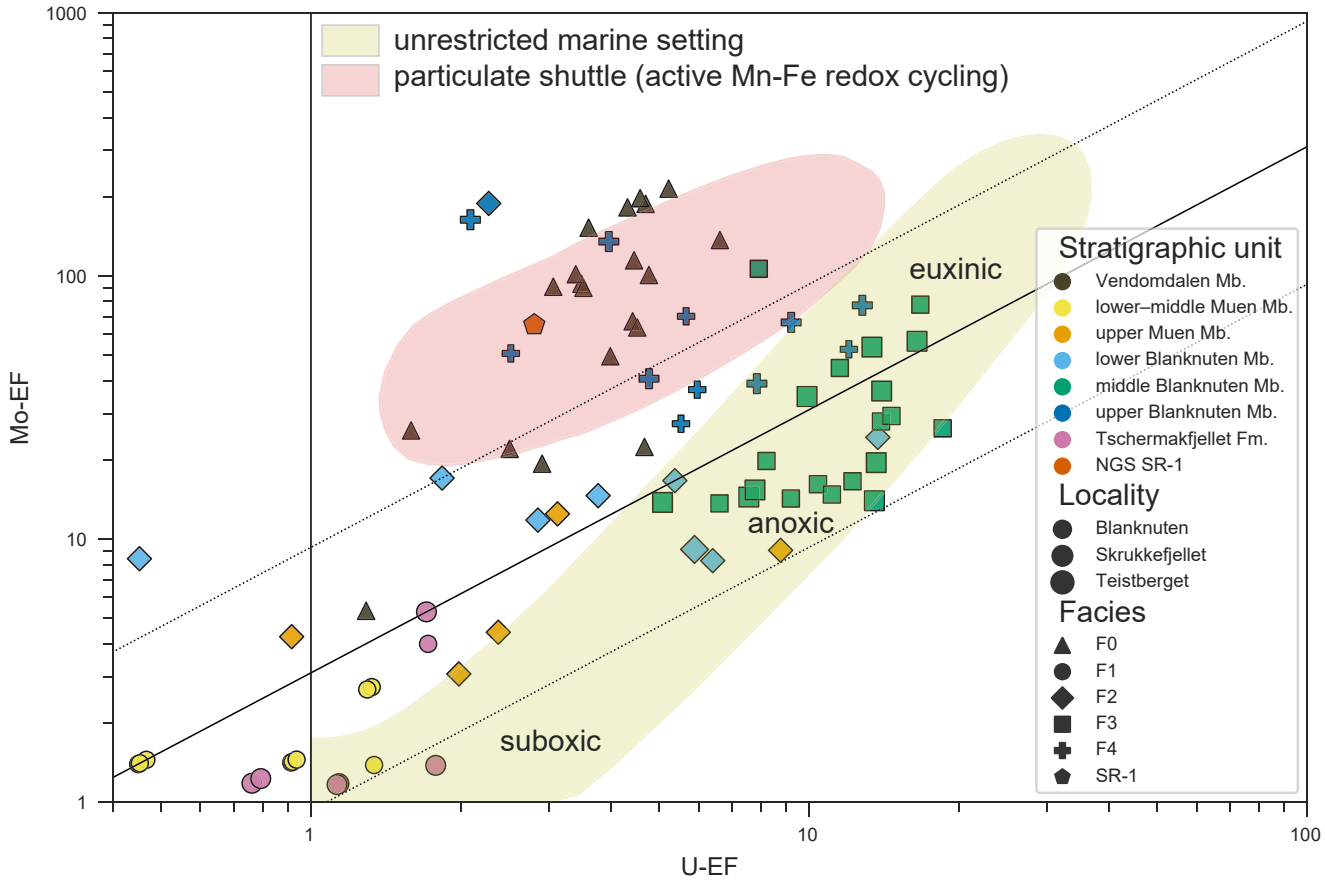

FIGURE 12 Cross plot of U-EF vs Mo-EF. The particulate shuttle field, unrestricted marine field and the diagonal solid line representing modern-day seawater U/Mo ratio = 3.1 (wt/wt) are taken from Tribovillard et al. (2012) and based on Algeo and Tribovillard (2009). The dotted diagonal lines represent multiples of 0.3 and 3

therefore mark the onset and development of matrix-supported phosphogenesis, reflecting enhanced upwelling of nutritious deep marine water and elevated productivity (Krajewski, 2008, 2013). The productivity proxies above provide valid criteria to chemostratigraphically distinguish these F2 mudstones from the underlying F1 mudstones (Figures 6 through 9).

The persistently high enrichment in TIC, TOC and EFs of Si, Ba, P, Ni and Cu in the middle Blanknuten Member F3 mudstones indicates deposition during periods with the most intense and prolonged primary productivity of all the studied facies types. The increased enrichment in the geochemical nutrient trinity Si-EF, P-EF and TOC is common for major marine phosphorite deposits (Kolodny, 2009). The elevated Si-EF in these F3 mudstones probably reflects the abundant radiolarian moulds reported in these mudstones (Bernhardsen, 2019; Krajewski, 2013). Conversely, the overall depleted Al (%) and Ti (%) (Figure 9B) and the conservative lithogenic elements K, Ga, Rb, Nb, Th (Appendix S1) in these F3 mudstones (Figure 9B) indicate low detrital input during the early Ladinian. These proxies thus coincide with former work that considered the F3 mudstones to represent deposition during a highstand phase, including the maximum flooding surface of the Middle Triassic 2nd order TR-sequence (Krajewski, 2008, 2013).

The relative decrease in all the EFs above except TIC in the upper Blanknuten Formation F2/F4 mudstones suggests that primary productivity generally decreased with the onset of the regressive phase in the late Ladinian. The serrated nature of the TOC, Si-EF and Ba-EF logs in these F2/F4 mudstones may correspond with short bursts of intense productivity related to algal blooms (Krajewski, 2013; Vigran et al., 2008). The TIC probably represents the abundant micro-coquina shell deposits previously reported within this unit (Mørk & Bromley, 2008). However, due to the possibly reworked nature of this stratigraphic unit and reported mass mortality events of juvenile bivalves (Krajewski, 2008, 2013; Mørk & Bromley, 2008), the TIC content does not necessarily reflect the productivity rate.

The strong correlation between the EFs of the rare earth elements (REEs) Sc, Y, La and Ce with P-EF (Figures 4 through 8) shows that the P-rich mudstones (F2–F4) are the most important hosts for REEs. Indeed, REEs are typically scavenged from the sea water during authigenic phosphate formation (Tribovillard et al., 2006). Furthermore, carbonate fluorapatite is by far the dominant phosphate

mineral in the Botneheia Formation (Krajewski, 2008). As the mineral lattice of carbonate fluorapatite is compatible with REEs (Jarvis et al., 1994), it appears that the enrichment in REEs is directly tied to the abundance of carbonate fluorapatite.

The Tschermakfjellet Formation F1 mudstones record a termination of all the productivity proxies above. This demarcates that upwelling-induced nutrient supply and phosphogenesis ceased in the early Carnian in eastern Svalbard.

5.3 | Palaeoredox regimes

Degradation of organic matter by scavengers and bacteria in aerobic conditions is relatively quick and efficient, resulting in oxidised and less lipid-rich OM (Demaison & Moore, 1980). In contrast, decomposition under anaerobic conditions, which is mostly due to bacterial activity, is less efficient and typically results in increasingly reduced (i.e. more C-H bonds) and lipid-rich OM with increased oil potential (Demaison & Moore, 1980). The benthic redox conditions are therefore closely tied to the preservation potential of reactive OM. In this study, the palaeoredox conditions for the defined mudstone facies (F0–F4) are reconstructed using TOC, TS, DOP_T and EFs of the redox-sensitive elements V, Cr, Fe, Co, Zn, As, Mo, Pb and U (Algeo & Li, 2020; Algeo & Liu, 2020; Algeo & Maynard, 2004; Tribovillard et al., 2006).

The planar lamination, weathered pyrite nodules and lack of bioturbation suggest impeded benthic oxygen supply as the Vendomdalen Member F0 mudstones were deposited. These mudstones show an affinity for sulphide-related redox proxies (EFs of Co, Fe, Mo, Pb, As) as demonstrated by the EFC3 (Figure 6) and PC2 (Figures 7 and 8), indicating that they were deposited during sulphate-reducing conditions. The Mo content for these F0 mudstones (mean 71 $\pm$ 46 ppm, SD) in combination with DOP values of the Vendomdalen Member (mean 0.43 $\pm$ 0.07, SD) from Krajewski (2013) further indicate frequent and intermittent euxinia (Scott & Lyons, 2012). This corroborates with Spathian euxinia reported in western and central Spitsbergen (Grasby et al., 2020; Hammer et al., 2019; Wignall et al., 2016; Xu et al., 2012) and Arctic Canada (Grasby et al., 2013, 2016). Upper Olenekian—presumably Spathian—mudstones on the New Siberian Islands are similar to the mudstones of the Spathian Vikinghøgda Formation in eastern Svalbard (Pčelina & Korčinskaja, 2008), further supporting a synchronous, regional Spathian anoxic event along the northern Pangea margin. As discussed by Grasby et al. (2016), this was possibly triggered by high ocean temperatures caused by the Early Triassic hothouse setting (Sun et al., 2012). On Edgeøya, this resulted in prolonged periods with depleted oxygen conditions favourable for extensive OM preservation (Figure 9).

The abrupt decline in the redox-sensitive element EFs (V, Fe, Co, Ni, Cu, As, Mo, Pb and U), TOC and TS in the Anisian lower–middle Muen Member F1 mudstones strongly indicates that the Spathian benthic euxinia on Edgeøya did not continue into the Anisian (Figure 8). Previously reported *Chondrites* and *Helminthopsis* trace fossils and OM–apatite–pyrite relationships in these F1 mudstones suggest oxygenated and hospitable sea floor conditions as they were deposited (Krajewski, 2013; Wesenlund et al., 2021). This contrasts Vigran et al. (2014) and Lundschien et al. (2014), who considered the entire Muen Member on Edgeøya to represent mudstones deposited during restricted and dominantly benthic anoxic conditions. The Cr-EF remains the only redox-sensitive proxy with a positive excursion across the VenMb–MueMb boundary (Figure 9). Interestingly, Algeo and Maynard (2004, their figure 6a) show that euxinic conditions may result in Cr depletion relative to anoxic (non-sulphidic) conditions at equal TOC values. Thus, the positive Cr-EF excursion directly above the VenMb–MueMb boundary is consistent with a change from euxinic to oxic/dysoxic benthic conditions. However, Cr enrichment is reported to be strongly affected by the land-derived clastic fraction and/or be enriched in carbonate fluorapatite (Tribovillard et al., 2006). The observed Cr-EF excursion could thus be unrelated to palaeoredox variations (Figure 9).

The upper Muen Member F2 mudstones up to the middle Blanknuten Member F3 mudstones mark a strong positive trend in EFs of Cr, Zn, V, As, U, but also TOC, TS and DOP_T (Figures 6 through 9). This is also captured convincingly by PC1 (Figure 8) and the DOP curve from Krajewski (2013, their figure 21). This indicates that the F2 mudstones of the upper Muen/lower Blanknuten members were deposited in less oxic (dysoxic) conditions compared to the underlying F1 mudstones of the lower–middle Muen Member. The overall high enrichment in the redox-sensitive elements in the middle Blanknuten Member F3 mudstones above thus implies that this facies was deposited during greater oxygen depletion, probably triggered by excessive benthic oxygen demand. This agrees well with Krajewski (2008, 2013), who interpreted the facies development within the lower–middle Muen Member to the middle Blanknuten Member interval to indicate deposition under progressively increasing primary productivity and OM sedimentation, ultimately forming a widespread OMZ.

The transition into the upper Blanknuten Member F2/F4 mudstones shows variable but overall decreasing concentrations in TOC, TS and EFs of U, Cr, V, indicating deposition during more oxic conditions relative to the underlying F3 mudstones. Abundant *Thalassinoides* burrows

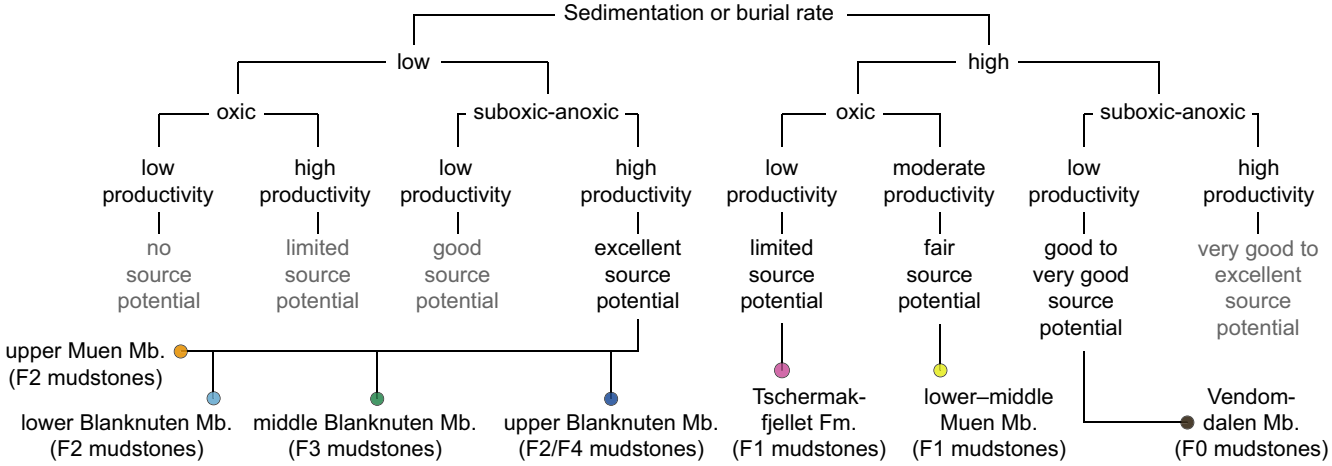

FIGURE 13 Flowchart of the three primary factors controlling source rock development and their relative influence on the Spathian–Carnian source rock potential in Svalbard. Grey text represents combinations that are generally not met by the studied units. Feedback loops are not considered. Based on Isaksen and Bohacs (1995); Katz (2005, their figure 1)

within these mudstones show that the O_2–H_2S boundary must have been frequently below the sediment–water interface during deposition (Krajewski, 2013; Mørk & Bromley, 2008). However, this does not explain the increase in Mo-EF in these F2/F4 mudstones, which in fact suggests euxinic conditions (Figure 9). This contrasts with Krajewski (2013), who only considered the middle Blanknuten Member to display benthic euxinia within the entire Botneheia Formation.

The cessation of the EFs of U and Mo (and TOC) across the BlaMb–TschFm boundary marks the onset of the well-ventilated, oxic Tschermakfjellet Formation F1 mudstones. This formation is overall poor in pyrite but is enriched in siderite cement and siderite nodules (Krajewski, 2013; Mørk et al., 1982). The elevated Co-EF (Figure 9) appears thus to reflect the siderophile properties of this element rather than reduced oxygen conditions.

5.4 | Water mass restriction

The relationship between U, Mo and TOC (Figure 9) enrichment in mudstones and the ratios Mo/U and Mo/TOC (Figures 10 and 11) are used to evaluate restricted vs. unrestricted benthic water masses in modern and ancient basins (Algeo & Lyons, 2006; Algeo & Maynard, 2008; Algeo & Rowe, 2012; Algeo & Tribovillard, 2009; Tribovillard et al., 2012). Uranium is primarily enriched under suboxic or less oxygen-rich conditions (i.e. in reducing conditions without the requirement of free H_2S) and is only scavenged within the sediment (Algeo & Maynard, 2004; Algeo & Tribovillard, 2009). However, in non-sulphidic anoxic conditions, U strongly correlates with TOC, exemplifying that U enrichment is not necessarily proportional to redox potential (Algeo & Maynard, 2004).

Similarly, Mo can be scavenged at or below the sea floor but requires the presence of H_2S (Helz et al., 1996, 2011). Strong Mo enrichment relative to U (i.e. 3–10 times greater than seawater Mo/U weight/weight concentrations) relies on active Mn-Fe redox cycling that effectively 'pumps' Mo into the sediments, and is most efficient when the O_2–H_2S boundary frequently fluctuates above and within the sediment–water interface (Tribovillard et al., 2012). Furthermore, while the Mo/TOC ratio is a commonly used water mass restriction proxy, it cannot

FIGURE 14 Simplified conceptual depositional model of the Spathian–Carnian (A through F; details are discussed in Section 5.6) mudstone succession in W (western), C (central) and E (eastern) Svalbard demonstrating how fluctuations in primary productivity, benthic redox and terrigenous flux influenced source rock richness and quality. TOC and HI are based on immature, oil-prone samples of the Vendomdalen Member in eastern Svalbard collected from Bjorøy et al. (2009) (see Figure 15 for explanation), while the TOC and HI data for the subunits of the Botneheia Formation and the Tschermakfjellet Formation are from immature to early mature samples on western and northern Edgeøya collected from Krajewski (2013). Note the similar relative change in TOC compared to Figure 10. The position of the delta top and delta front in the west is based on Bjerager et al. (2019); Glørstad-Clark et al. (2010); Klausen et al. (2015); Lundschien et al. (2014); Riis et al. (2008). Relative sea-level changes and occurrence of an OMZ are based on Krajewski (2008, 2013). Ages of the Botneheia and Steinkobbe formations are collected from Hounslow et al. (2008); Krajewski and Weitschat (2015); Vigran et al. (1998, 2014). The correlated lithostratigraphy and chronostratigraphy should be considered approximate and relative as the informal subunits of the Botneheia Formation and their respective boundaries exhibit a variable degree of diachronicity (Krajewski, 2008). The implied benthic palaeoredox conditions are only covered for the Edgeøya region where the data coverage is sufficient

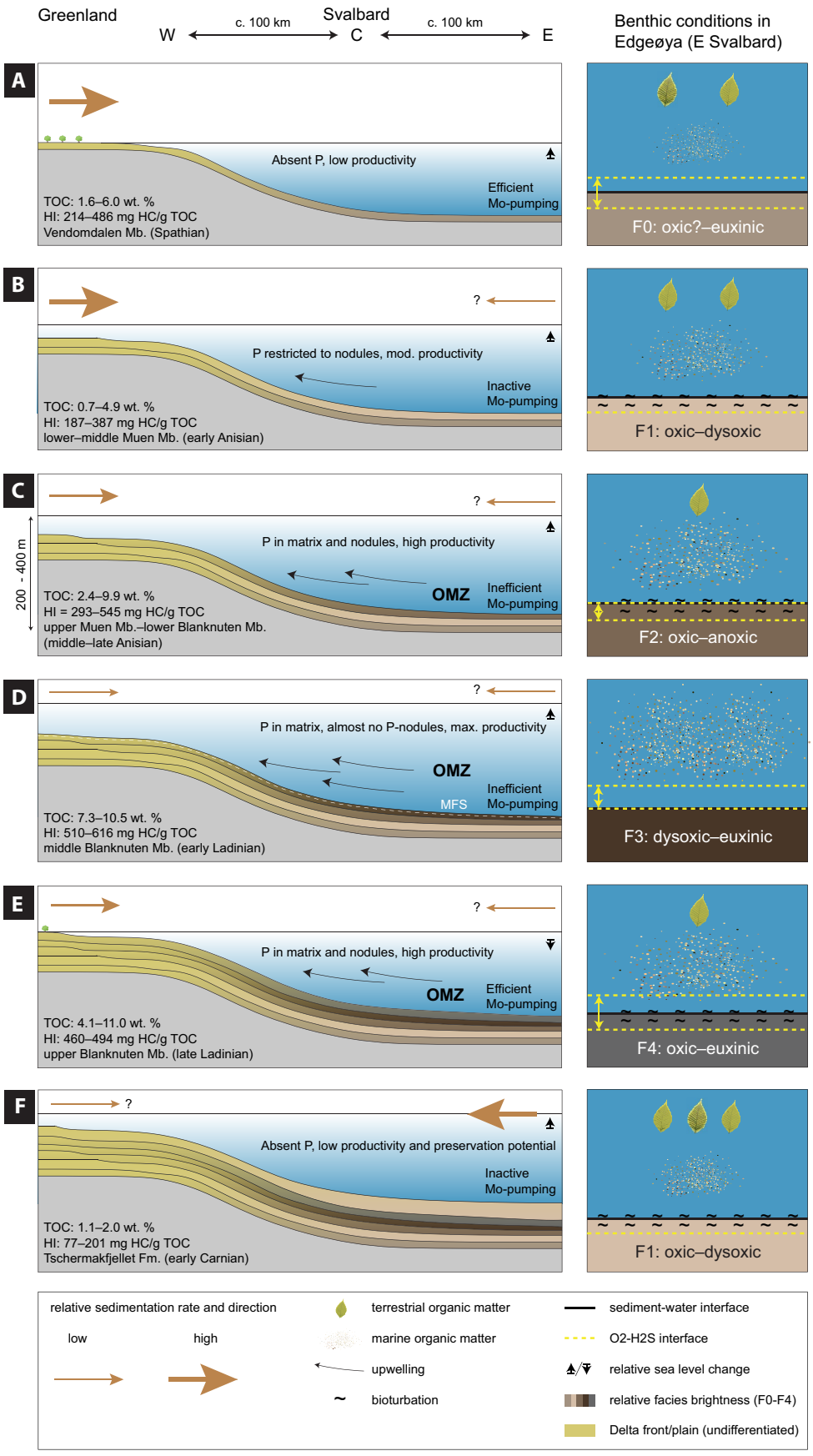
Greenland
W
c. 100 km
Svalbard
C
c. 100 km
E
Benthic conditions in Edgeøya (E Svalbard)
A
Absent P, low productivity
Efficient Mo-pumping
TOC: 1.6–6.0 wt. %
HI: 214–486 mg HC/g TOC
Vendomdalen Mb. (Spathian)
F0: oxic?–euxinic
B
?
P restricted to nodules, mod. productivity
Inactive Mo-pumping
TOC: 0.7–4.9 wt. %
HI: 187–387 mg HC/g TOC
lower–middle Muen Mb. (early Anisian)
F1: oxic–dysoxic
C
200 - 400 m
P in matrix and nodules, high productivity
OMZ
Inefficient Mo-pumping
TOC: 2.4–9.9 wt. %
HI = 293–545 mg HC/g TOC
upper Muen Mb.–lower Blanknuten Mb.
(middle–late Anisian)
F2: oxic–anoxic
D
P in matrix, almost no P-nodules, max. productivity
OMZ
MFS
Inefficient Mo-pumping
TOC: 7.3–10.5 wt. %
HI: 510–616 mg HC/g TOC
middle Blanknuten Mb. (early Ladinian)
F3: dysoxic–euxinic
E
P in matrix and nodules, high productivity
OMZ
Efficient Mo-pumping
TOC: 4.1–11.0 wt. %
HI: 460–494 mg HC/g TOC
upper Blanknuten Mb. (late Ladinian)
F4: oxic–euxinic
F
Absent P, low productivity and preservation potential
Inactive Mo-pumping
TOC: 1.1–2.0 wt. %
HI: 77–201 mg HC/g TOC
Tschermakfjellet Fm. (early Carnian)
F1: oxic–dysoxic
relative sedimentation rate and direction
low
high
terrestrial organic matter
marine organic matter
upwelling
bioturbation
sediment-water interface
O2-H2S interface
relative sea level change
relative facies brightness (F0-F4)
Delta front/plain (undifferentiated)

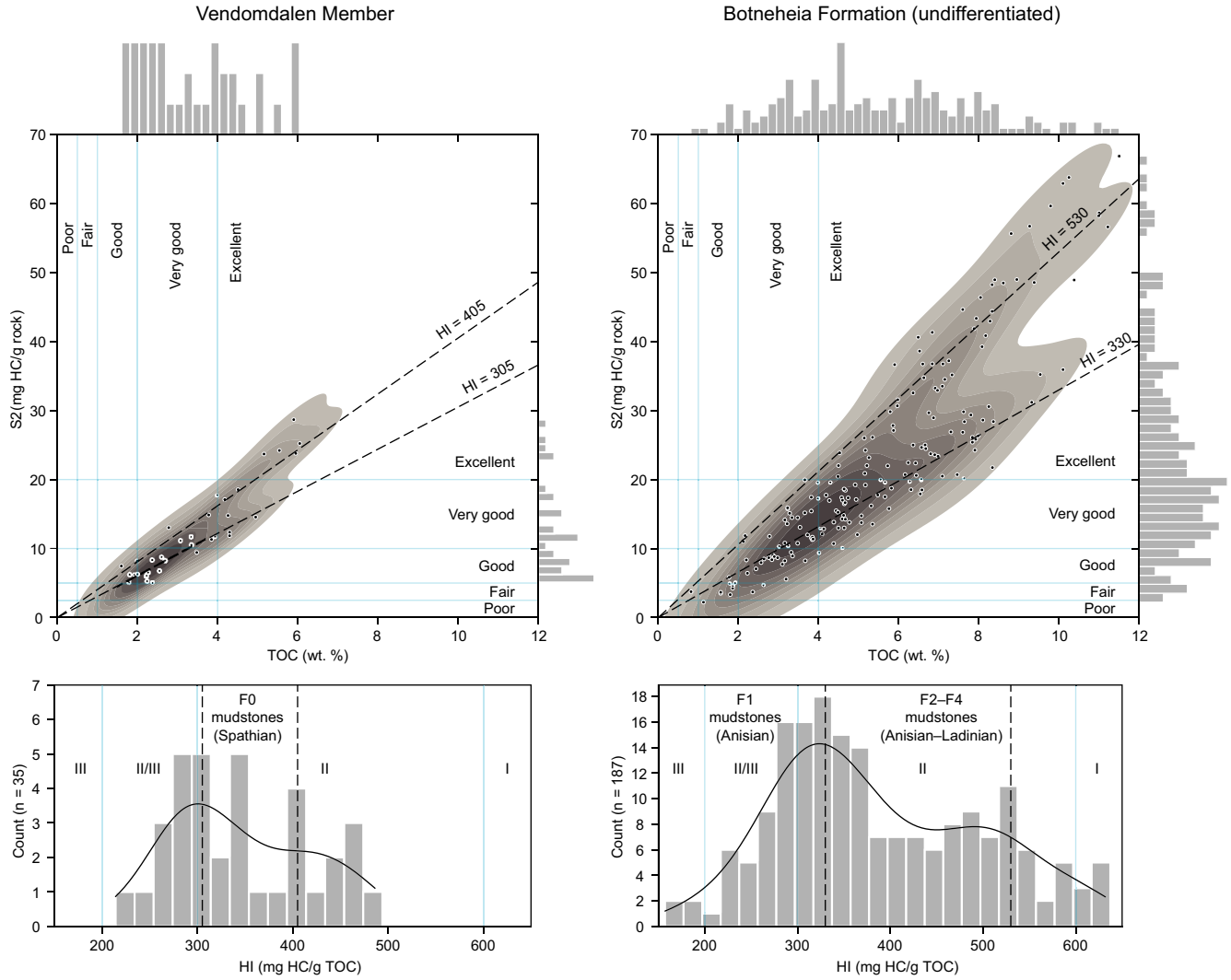

FIGURE 15 Scatter plots, histograms and kernel density estimates of TOC, S_2 and HI (Rock-Eval 6) of immature and oil-prone samples from the Vikinghøgda ($n = 35$) and Botneheia ($n = 187$) formations. The data was collected from Bjorøy et al. (2009, their figure 3a) using the WebPlotDigitizer data extraction software (Rohatgi, 2020). Bjorøy et al. (2009) did not differentiate the data based on members or facies. As only the Vendomdalen Member of the Vikinghøgda Formation is considered oil prone (kerogen type II/III) (Mørk et al., 1999), it is assumed that all the plotted Vikinghøgda Formation samples are from this member. The HI isolines = 305 and 405 mg HC/g TOC highlight the positively skewed HI distribution. The lower–middle Muen Member F1 mudstones are considered kerogen type II/III mudstones, while the mudstones of the upper Muen–Blanknuten members (F2–F4) are kerogen type II (Krajewski, 2013). The bimodal HI distribution for the Botneheia Formation and the two HI isolines at 330 and 530 mg HC/g TOC may reflect representative, typical HI values for immature and oil-prone non-phosphogenic (F1) and phosphogenic (F2–F4) mudstone facies respectively

be applied to unrestricted upwelling systems as oxygen depletion in such settings may be controlled by variable primary productivity rather than hydrogeographic effects (Algeo & Rowe, 2012).

The variable U enrichment (Figures 8 and 9) will affect the gamma ray (GR) expression of the studied mudstone section. A synthetic GR log is included (Figure 10) for interpretation and correlation to offshore Lower–Middle Triassic mudstone equivalents (i.e. the Steinkobbe Formation; see Section 5.6). The GR log was calculated from U, Th and K (Ellis & Singer, 2007, their equation 11.1): $GR_{API} = 8 \times U + 4 \times Th + 16 \times K$, where GR is given in API units, and U, Th and K are given in ppm, ppm and % respectively. The geochemical logs of U (ppm), Th (ppm) and K (%) are available in Appendix S1.

The Mo/TOC ratios of the Vendomdalen Member F0 mudstones are mostly comparable to Mo/TOC trend of the modern-day Saanich Inlet in western Canada (Figure 11), which is a seasonally euxinic basin (Algeo & Lyons, 2006; Francois, 1988). The Mo vs. TOC plot (Figure 11) and the Mo-EF vs. U-EF (Figure 12) plot of the Vendomdalen Member F0 mudstones also correlate to the uppermost Albian–lowermost Campanian La Luna Formation source rock (Maracaibo Basin, Venezuela) that was

deposited in a basin bounded by shallow sills and during the Cenomanian–Turonian OAE-2 and the Coniacian–Santonian OAE-3 (Mongenot et al., 1996; Tribovillard et al., 2012). Overall, this suggests that Mn-Fe redox cycling was highly effective and caused Mo-enriched muds during deposition of these F0 mudstones. Similarly, Chen et al. (2019) report active Mn–Fe redox cycling constrained to a mid-Spathian section (Chaohu, east China) deposited in the Early Triassic eastern palaeo-Tethys Ocean. Zhang et al. (2018) suggest that global benthic anoxia was particularly evident at the Spathian–Anisian transition, termed the C4 event. It may thus be speculated that the strong and upwards increasing Mo enrichment in the Spathian Vendomdalen Member F0 mudstones (Figure 9) formed due to global ocean stratification that promoted worldwide intermittent benthic euxinia.

However, the observed euxinia and interpreted weak water mass restriction during deposition of the Vendomdalen Member F0 mudstones could be due to local relief related to inherited bathymetry caused by underlying Upper Palaeozoic fault blocks (Anell et al., 2016; Steel & Worsley, 1984). At a regional scale, a structurally controlled bedrock sill located between the Alaska-Chukotka microcontinent (also known as Crockerland; see Embry, 1993) and Arctic Canada could hypothetically enable a silled or restricted basin setting for the entire TBO (Leith et al., 1993; Sømme et al., 2018). The Bosporus Strait, which serves as a narrow connection between the restricted Black Sea and the less restricted Mediterranean Sea, is a modern example of such a silled basin setting (Demaison & Moore, 1980). However, the high Mo/U and Mo/TOC ratios (Figures 10 and 11) and Mo-EF vs U-EF (Figure 12) recorded in this study do not suggest such an extreme restriction compared to that of the Black Sea, which has significantly lower Mo/U and Mo/TOC ratios (cf. Algeo & Lyons, 2006; Algeo & Tribovillard, 2009).

The Mo-EF, U-EF, TOC, Mo/U and Mo/TOC ratios abruptly decrease above the VenMb–MueMb boundary (Figures 9, 10 and 11), indicating that the Anisian lower–middle Muen Member F1 mudstones were deposited in oxygenated and ventilated waters relative to the Vendomdalen Member F0 mudstones. The VenMb–MueMb boundary denotes a regional early Anisian flooding event (Mørk et al., 1989) and represents the onset of rising sea level that probably enhanced the physical connection between the Boreal Ocean and the deep Panthalassic Ocean during the early Anisian, promoting mixing of shelf waters with nutritious upwelling water masses (Krajewski, 2008, 2013). A cooling climate during the Middle Triassic probably raised the thermocline to a substantially shallower position, also resulting in improved oxygen conditions in the basin (Grasby et al., 2016, 2020).

The Mo-EF and U-EF relationship in the Anisian upper Muen Member mudstones (F2) and Anisian–Ladinian lower–middle Blanknuten Member mudstones (F2–F3) indicates a hydrodynamically unrestricted marine setting (Figure 12). The observed coupling between redox and productivity proxies (Figures 6 through 9), strongly suggests that the recorded oxygen depletion was promoted by a growing primary production, organic sedimentation and benthic oxygen consumption caused by high nutrient availability due to the increasing influx of deep marine water from the Panthalassic Ocean. The Mo-EF and U-EF trends of these F2 and F3 mudstones directly overlap with those of the Upper Jurassic Kashpir oil shales of the Russian Platform (Riboulleau et al., 2003; Tribovillard et al., 2012). The Kashpir oil shales were deposited in an epicontinental unrestricted marine environment characterised by high primary productivity and frequently fluctuating oxic to anoxic conditions (Riboulleau et al., 2003). High concentrations of redox-sensitive elements and TOC within the intensively burrowed but oil-prone Kashpir mudstones show that the redox boundary was close to the sediment-water interface and frequently within the sediment during deposition. A similar depositional setting has also been suggested for the mudstones of the upper Muen and the lower Blanknuten members (Krajewski, 2008, 2013).

The Ladinian middle Blanknuten Member F3 mudstones indicate deposition during maximum primary productivity and in euxinic bottom waters (Figures 8, 9 and 12), suggesting that benthic OM degradation stalled as oxygen demand exceeded the supply. Neither this study or that of Wesenlund et al. (2021) documented bioturbation in these F3 mudstones. However, thin, but common, peloidal packstone layers provide evidence of hydrodynamic activity in this unit (Krajewski, 2013). Vigran et al. (2014) reported abundant *Daonella* bivalves in the middle Blanknuten Member mudstones. *Daonella* bivalves probably lived on top of the soft sediment as 'snowshoe' strategists (Schatz, 2005), indicating short, recurrent periods of habitable benthic bottom waters despite the prevailing oxygen deficient environment. The inefficient or even inactive Fe–Mn redox cycling as indicated by the Mo-EF vs U-EF ratio (Figure 12) also supports that the redox boundary was fluctuating at the sediment–water interface and above, but rarely (or never) within the sediment, in agreement with Krajewski (2013).

The upper Ladinian upper Blanknuten Member F2/F4 mudstones mark the reintroduction of efficient Mn-Fe redox cycling and Mo enrichment comparable to the Vendomdalen Member mudstones (Figure 12), indicating that the upper Blanknuten Member F4 mudstones were largely deposited during intermittent benthic euxinia. This contrasts with the findings of Krajewski (2013),

who interpreted true euxinic conditions to have only occurred during deposition of the middle Blanknuten Member F3 mudstones. The upper Blanknuten Member F2/F4 mudstones were probably deposited in a gradually shallowing environment, which experienced a stepwise change from euxinic to dysoxic conditions due to water mass stirring and ventilation caused by the shoaling of the basin (Krajewski, 2008, 2013). This could have initiated a weakly restricted silled basin setting, possibly enhanced by undulating bottom morphology if present. The regressive development and the relative position to the approaching TBO delta system or Greenland to the west probably increased the influx of fresh water and riverine nutrients as indicated by common terrestrial organic matter within this unit (Krajewski, 2013). The influx of riverine water and nutrients could have triggered algal blooms of *Tasmanites* and resulted in brackish waters and formation of halocline/thermocline stratification (Høy & Lundschien, 2011; Vigran et al., 2008), promoting water mass restriction in the basin without the aid of underlying bathymetry.

The lowermost Tschermakfjellet Formation F1 mudstones denote an abrupt termination of elevated Mo/TOC and Mo/U ratios (Figures 11 and 12). The onset of oxygenated conditions that prevailed in the early Carnian during deposition of these F1 mudstones may have been caused by oceanographic reconfiguration that lowered the preservation potential following the base Carnian flooding (Høy & Lundschien, 2011).

5.5 | Influences on the non-biogenic mineral fraction

The EFC1 from the HCA (Figure 6; Table 4) and the dominant element EFs with positive loadings on PC3 (Figure 8) contain several elements (Ga, Rb, Cs, Th, K, Ti, Nb) that are commonly associated with non-carbonate minerals (cf. Craigie, 2015, 2018). Variations in EFC1 and PC3 (except for TIC and Mg) appear therefore to be influenced by changes in the non-biogenic mineral fraction. The variations in EFC1 and PC3 could therefore provide important information on the resulting rock composition due to, for example varying detrital grain size, switching provenance area, palaeoweathering or authigenic mineral precipitation (Boës et al., 2011; Craigie, 2015, 2018; Craigie et al., 2016; Rothwell & Croudace, 2015).

Both Ga and Cs are typically correlated with clay minerals and feldspars, and Nb and Th with heavy minerals (Craigie, 2018). Aluminium, K and Rb are principally associated with aluminosilicate minerals (i.e. clays) (Calvert & Pedersen, 2007), but K is also hosted by K-feldspar (Craigie, 2018). Titanium is often assigned to represent silt-sized Fe-rich clastic mineral particles (Rothwell & Croudace, 2015). Zirconium is almost exclusive to zircons (Craigie, 2018), and the Zr/Al ratio (Zr-EF in this study) is useful as a grain-size proxy as zircons commonly show grain sizes coarser than clays (Atar et al., 2019; Liang et al., 2013; Pang et al., 2018). Sodium is linked with smectite, plagioclase or halite (Craigie, 2018); however, halite is an improbable mineral to occur within the studied mudstone succession as the depositional environment in eastern Svalbard was a shallow–open marine shelf during the Early–Middle Triassic (Figure 2). Consequently, the stratigraphic variations in EFC1 (Figure 6) and PC3 (Figures 7 and 8)—including Zr-EF and Na-EF but excluding TIC and Mg—appear to mainly record compositional changes between clay minerals, feldspars and heavy minerals. The significant vertical changes in the EFs of Na, K, Ti, Ga, Rb, Zr, Nb, Cs and Th across the regionally extensive VenMb–MueMb or BlaMb–TschFm lithostratigraphic boundaries therefore confirm the chemostratigraphic significance of these elements (Figures 8 and 9; Appendix S1).

The negative shifts in Na-EF and Zr-EF but positive shifts in Rb-EF and Cs-EF across the VenMb–MueMb boundary (Figures 8 and 9; Appendix S1) correspond to the transition from coarser-grained (F0) to finer-grained (F1) mudstones seen on Edgeøya (Krajewski, 2008; Vigran et al., 2014; This study). This chemostratigraphic boundary thus correlates to the previously reported earliest Anisian flooding event and associated relative decrease in grain size and sedimentation rate (Mørk et al., 1994; Vigran et al., 2014). Spathian–early Anisian sedimentation rates in Svalbard were both relatively higher compared to the late Anisian–Ladinian (Hounslow et al., 2008a). Consequently, these variations do not appear to reflect a change in provenance area, as the muds that eventually formed the Vikinghøgda and Botneheia formations on Edgeøya were both dominantly sourced from the west, i.e. Greenland (Gilmullina et al., 2021; Mørk et al., 1982).

The significant decrease in the Ti-, Nb-, Rb- and Zr-EFs across the BlaMb–TschFm boundary also points to a decrease in relative grain size. As PC3 increases upwards within the Botneheia Formation (Figure 8), the upper Blanknuten Member F2/F4 mudstones appear to record the coarsest mudstones within this formation. This may reflect increased sediment influx during the regressive phase of the Middle Triassic TR-sequence following the Ladinian highstand phase (F3 mudstones) or increased hydrodynamic reworking and winnowing related to shallower water depths (Krajewski, 2013; Mørk et al., 1982, 1989). The relative increase and decrease in Na-EF and K-EF above this boundary could suggest that plagioclase (Na-rich) became more abundant relative to K-feldspar (K-rich) (Figure 8). However, dedicated mineralogical analyses are necessary to confirm the proposed

element:mineral links as authigenic mineral precipitation may overprint the detrital mineral signature (Craigie, 2018). Still, Uralian-sourced sands from Anisian and Carnian deposits on the southern Barents Shelf host abundant plagioclase (Fleming et al., 2016; Line et al., 2018), while age-equivalent Caledonian-derived sands typically comprise less feldspars, although with relatively more K-feldspar (Fleming et al., 2016). This could indicate that the Tschermakfjellet Formation F1 mudstone samples in SC4 (low Na-EF, high K-EF; Figure 6) are still dominantly Caledonian (from NW–W), while the overlying SC2 F1 mudstone samples from the same formation (High Na-EF, low K-EF; Figure 6) are dominantly Uralian-sourced (from E–SE) (cf. Fleming et al., 2016; Line et al., 2018). The lowermost Tschermakfjellet Formation F1 mudstones could therefore have been deposited during a gradually increasing influx of Uralian sediments that eventually became the dominant provenance in eastern Svalbard during the early Carnian (Bue & Andresen, 2014; Gilmullina et al., 2021).

5.6 | Source rock potential and regional correlation

A flowchart of important variations in source rock-forming processes (discussed in Sections 5.2–5.5) is proposed for each stratigraphic unit and their resulting source potential (Figure 13) (based on Katz, 2005, their Figure 1). From the proxies discussed above and the flowchart, a conceptual depositional model is presented for the Spathian–Carnian succession in eastern Svalbard (Figure 14). The relative source rock potential between the Vendomdalen, lower–middle Muen and the upper Muen/entire Blanknuten members (Figure 14) fits well with replotted TOC-S_2 and HI data from Bjorøy et al. (2009) (Figure 15). This shows that immature and oil-prone mudstones within these stratigraphic units have intermediate, lower and higher oil generation potential respectively.

According to Lundschien et al. (2014), the mudstones of the Spathian–Anisian Steinkobbe Formation in the Svalis Dome, southern Barents Sea (Figure 1) are facies equivalent (i.e. of the same palaeodepositional environment but time-transgressive) to those of the Anisian–Ladinian Botneheia Formation in Svalbard. The Spathian Vendomdalen Member of the underlying Vikinghøgda Formation in Svalbard is typically excluded in all these types of comparisons (Lundschien et al., 2014; Lutz et al., 2021; Norwegian Petroleum Directorate, 2017; Riis et al., 2008). A discussion on the correlation, source potential and regional distribution of the onshore and offshore Spathian to Ladinian (and Carnian) successions follows below.

Immature and oil-prone Spathian Vendomdalen Member F0 mudstones in eastern Svalbard show liquid hydrocarbon generation potential (Figure 15) (mean HI = 346 ± 73 mg HC/g TOC, SD) almost identical to the Spathian lower Steinkobbe Formation in the Svalis Dome (core 7323/07-U-04 and 7323/07-U-03; mean HI = 346 ± 116 mg HC/g TOC, SD) (Abay et al., 2018). Both units are largely unbioturbated (Table 3; Mørk & Elvebakk, 1999). In the Blanknuten locality, the upper part of the Vendomdalen Member F0 mudstones probably encompass the Upper Spathian *Jerseyiaspora punctispinosa* palynozone, although the lower F0 mudstones may include the early Spathian *Pechorosporites disertus* palynozone (Vigran et al., 2014). In the Svalis Dome, the lower (but not lowermost) Steinkobbe Formation is also specifically assigned to the *J. punctispinosa* palynozone (Vigran et al., 2014). Thus, the Spathian period may have seen elevated preservation potential that was fairly synchronised throughout the TBO. This could have been triggered by sluggish water mass circulation causing benthic euxinia (Figure 15A) due to the Early Triassic hothouse conditions (Grasby et al., 2016, 2020) rather than nutrient-driven productivity (upwelling or fluvial) and oxygen demand. This would explain why the uppermost Spathian mudstones of the lower Steinkobbe Formation (core 7323/07-U-04) host far less phosphate nodules compared to the Anisian mudstones of the upper Steinkobbe Formation (core 7323/07-U-01 and 7323/07-U-09) (Mørk & Elvebakk, 1999, their figure 10).

Immature and oil-prone lower–middle Muen Member F1 mudstones in eastern Svalbard (implied mode HI *ca* 320–340 mg HC/g TOC) (Figure 15) and the lowermost Anisian mudstones in the Steinkobbe Formation (core 7323/07-U-04) are assigned to the early Anisian *Anapiculatisporites spiniger* palynozone (Vigran et al., 2014). While the lower Anisian F1 mudstones in Svalbard are OM-rich and record the onset of increased productivity from the underlying F0 mudstones (Figures 13 and 14), they still show relatively lower oil generation potential than the F0 mudstones, perhaps due to increased marine OM degradation and preferential preservation of terrestrial OM (Figure 14) (Wesenlund et al., 2021). Interestingly, the lower Steinkobbe Formation also shows a prominent decrease in TOC and GR response (Mørk & Elvebakk, 1999, their Figure 3) at the Spathian–Anisian boundary (compare with Figure 10), suggesting that early Anisian benthic oxygenation was regional in the TBO. In fact, Krajewski (2008, 2013) and Wesenlund et al. (2021) considered these lowermost Anisian F1 mudstones to have been deposited during well-ventilated shelf conditions. This would explain the lower organic richness in these mudstones (mean TOC = 1.58 ± 0.51 wt%, SD) compared to the underlying

F0 mudstones (mean TOC = 2.70 ± 0.79 wt%, SD) (Figure 9). The latter also exhibit a max. HI = 486 mg HC/g TOC which is not expected to be more than *ca* 400 mg HC/g TOC for the Anisian F1 mudstones (Krajewski, 2013). Lower Anisian F1 mudstones are therefore probably less oil-prone than the underlying upper Spathian mudstones throughout large parts of the Norwegian Barents Sea.

The phosphatic, oil-prone and bioturbated F2 mudstones of the upper Muen and most of the lower Blanknuten members in eastern Svalbard (Figure 14) are assigned to the middle Anisian *Triadispora obscura* palynozone (Vigran et al., 2014). In the same area, the F2 mudstones of the uppermost lower Blanknuten Member are assigned to the late Anisian *Protodiploxypinus decus* palynozone (Vigran et al., 2014). These F2 mudstones are therefore facies- and age-equivalent to the organic-rich, phospate nodule rich and bioturbated mudstones in core 7323/07-U-01 (*T. obscura* palynozone) and 7323/07-U-09 (*P. decus* palynozone) of the middle–upper Steinkobbe Formation (Vigran et al., 1998). The onset of intense middle Anisian phosphogenesis appears thus to be synchronous in the Triassic Boreal Ocean, perhaps triggered by the heightened water column and unrestricted waters that promoted upwelling and marine nutrient supply (Figures 13 and 14), ultimately forming an OMZ (Grasby et al., 2016, 2020; Krajewski, 2013). The middle–upper Anisian phosphogenic mudstones in the Svalis Dome are less oil-prone than their Svalbard counterparts (Abay et al., 2018), suggesting that middle–upper Anisian source rock potential increases northwards from the southern Barents Sea. This agrees with the common expectation of higher source rock potential towards the more distal parts of the TBO delta system clinoforms (Lutz et al., 2021).

The middle Blanknuten Member F3 mudstones in eastern Svalbard are assigned to the Ladinian *Echinitosporites iliacoides* palynozone (Vigran et al., 2014). These are highly oil-prone and were deposited during maximum drowning and maximum primary productivity, forming an extensive OMZ (Figure 14) (Krajewski, 2013). These F3 mudstones are age-equivalent to the deltaic and more proximal lower Snadd Formation (Tschermakfjellet Formation facies equivalent) in the Svalis Dome (cores 7323/07-U-10, 7323/07-U-05, 7323/07-U-02) (Vigran et al., 1998). Ladinian F3-type mudstones appear thus to be restricted to the northern Barents Sea, as the deep shelf conditions necessary for OM accumulation had ceased in the southeastern Barents Sea at that time (Figure 2) (Klausen et al., 2015). Still, the lateral distribution of the F3 mudstones is not known. Mapping their extent would provide important knowledge of their significance as source rocks in the areas open for commercial exploration in the Norwegian Barents Sea.

The oil-prone upper Blanknuten Member F2/F4 mudstones belong to the same palynozone as the F3 mudstones (Ladinian) and record the regressive phase of the Middle Triassic TR-sequence (Figure 14) (Krajewski, 2013; Vigran et al., 2014). According to Fleming et al. (2016, their figure 1), these upper Ladinian mudstones indicate less southeastward extent relative to the underlying F3 mudstones, possibly due to the gradually approaching TBO delta system (Figure 2). East of Kong Karls Land (Figure 1), immature upper Ladinian mudstones (core 7831/02-U-02) show excellent oil generation potential (mean HI =537 ± 34 mg HC/g TOC, SD), several phosphate nodules and relatively high and variable Mo/TOC ratios (1.34–28.13, mean 9.38 wt ppm/wt%) (Xu et al., 2014). These Mo/TOC ratios can only correspond with the upper Blanknuten Member in Edgeøya (Figure 10). Thus, the upper Ladinian F2/F4 mudstones and the benthic intermittent euxinia (Figure 14) may cover a 250 km SW–NE transect in the northern Barents Sea (Figure 2), suggesting that these late Ladinian palaeodepositional conditions were regional.

The progradation of the TBO delta system during the early Carnian (Figure 14) (Tschermakfjellet Formation F1 mudstones) effectively terminated the conditions to form organic-rich phosphatic mudstones in eastern Svalbard, in agreement with Lundschien et al. (2014). However, upwelling and primary productivity were still highly active towards the west in the North Slope Basin, northern Alaska, eventually forming the organic-rich and phosphatic mudstones of the Middle (not Lower) to Upper Triassic Shublik Formation (Parrish et al., 2001). The lack of Upper Triassic oil-prone phosphatic source rocks in the northern Norwegian Barents Sea is therefore linked with changes in depositional environment rather than climate-induced ocean reconfigurations as Upper Triassic phosphatic mudstones exist elsewhere in the TBO.

6 | CONCLUSION

This study combines sedimentological observations with a hitherto unexplored whole-rock multi-elemental chemostratigraphic framework of an excellently exposed Lower–Upper Triassic mudstone succession in eastern Svalbard, Arctic Norway. The contrasting elemental assemblages of the assigned lithostratigraphic units and their associated mudstone facies prove that whole-rock elemental chemostratigraphy is an effective tool to recognise principally different organic-rich Triassic mudstones with similar source potential. Abrupt elemental chemostratigraphic excursions at the tops of the circum-Arctic Lower and Middle Triassic 2nd order TR–sequences provide excellent criteria to map these important sequence stratigraphic boundaries in the northern Norwegian Barents Sea.

The mudstones of the studied Spathian–Carnian succession were deposited in an epicontinental basin in front of the developing TBO delta system, where the combined and complex interplay between primary productivity, benthic redox conditions, water mass restriction and sedimentation rate resulted in overall organic-rich mudstones, but of varying source rock quality and richness. The redox and productivity sensitive elemental chemostratigraphy were most importantly affected by (i) a deepened thermocline causing weak water mass restriction that lowered nutrient supply and productivity, but introduced intermittent benthic euxinia without observed bioturbation during Spathian hothouse conditions; (ii) introduction of well-ventilated, oxic/dysoxic, bioturbated benthic conditions with lowered preservation potential, but still an increase in upwelled nutrient supply that promoted moderate productivity and phosphate nodule formation following the regional earliest Anisian transgression; (iii) a gradual relative sea-level rise and developing upwelling and productivity causing increased oxygen consumption, matrix-wide phosphogenesis and subsequent suboxia/anoxia during the middle–late Anisian, although still with abundant tunnel burrows; (iv) sea-level high stand with intense primary productivity in the early Ladinian due to high nutrient supply from unrestricted upwelled waters, triggering maximum oxygen consumption and dominantly benthic euxinia without observed bioturbation; (v) regression and shallowing waters during the late Ladinian, resulting in weakly restricted water masses and frequent lowering of the O_2–H_2S interface below the sediment surface, thus reintroducing tunnel burrows, and; (vi) the base Carnian transgression, which mostly eliminated preservation of oil-prone organic matter as bottom waters became ventilated and oxic.

This study suggests that the Triassic upwelling-induced productivity and widespread phosphogenesis in front of the TBO delta system were not firmly established before the Anisian. The Spathian lower Steinkobbe Formation in the Barents Sea seems therefore genetically unrelated to the Middle Triassic Botneheia Formation in Svalbard. Further work on ocean circulation, nutrient supply, primary productivity and climate change across the Spathian–Anisian boundary in the Barents Sea may provide answers on the importance of climate change and delta development on Triassic source rock formation.

7 | COMPUTER CODE AVAILABILITY

- Name of code: Wesenlund_et_al_2022_TDR.py
- Developer: Fredrik Wesenlund
- Contact details: Fredrik Wesenlund, Department of Geosciences, UiT The Arctic University of Norway, Norway; email: fredrik.wesenlund@uit.no; Year first available: 2021
- Hardware used: The Python script was developed and run on a notebook PC with a quad core CPU @ 1.60–2.11 GHz and 16 GB RAM
- Software used and required: The Python script was developed with the Anaconda 2020.11 Python distribution platform (Anaconda, 2020) using Spyder 4.1.5 and needs the pandas, matplotlib, seaborn, scikit-learn and numpy packages
- Program language: the code is written in Python 3.8.7
- Total size of script: *ca* 11 KB
- Details on how to access the source code: the source file can be downloaded from GitHub: https://github.com/fredrwes/Publications

ACKNOWLEDGEMENTS

This study forms part of the ARCEx consortium (Research Centre for Arctic Petroleum Exploration) which is funded by the Research Council of Norway (grant number 228107) and ARCEx partners. We are grateful for additional economic support from Lundin Energy Norway and the Norwegian Petroleum Directorate for the field expedition to Edgeøya. Atle Mørk is thanked for field expedition planning, logistics, helpful discussions and great companionship, and the crew at research vessel SS Youexplore by The Dale Oen Experience for safe execution. Sofie Bernhardsen is acknowledged for field assistance and scientific contributions. Trine Dahl, Ingvild Hald and Karina Monsen are thanked for help and discussions in the geology lab at UiT–The Arctic University of Norway. Comments and suggestions by the Associate Editor Benjamin F. Walter and two anonymous reviewers on an earlier version of the manuscript are gratefully acknowledged.

CONFLICT OF INTEREST

The authors declare that they have no known competing financial interests or personal relationships that could have appeared to influence the work reported in this paper.

ORCID

Fredrik Wesenlund https://orcid.org/0000-0003-0433-4879
Sten-Andreas Grundvåg https://orcid.org/0000-0002-4309-898X

REFERENCES

Abay, T.B., Karlsen, D.A., Pedersen, J.H., Olaussen, S. & Backer-Owe, K. (2018) Thermal maturity, hydrocarbon potential and kerogen type of some Triassic-Lower Cretaceous sediments from the SW Barents Sea and Svalbard. *Petroleum Geoscience*, *24*, 349–373.

Algeo, T.J., Kuwahara, K., Sano, H., Bates, S., Lyons, T., Elswick, E., Hinnov, L., Ellwood, B., Moser, J. & Maynard, J.B. (2011) Spatial variation in sediment fluxes, redox conditions, and productivity in the Permian-Triassic Panthalassic Ocean. *Palaeogeography, Palaeoclimatology, Palaeoecology*, *308*, 65–83.

Algeo, T.J. & Li, C. (2020) Redox classification and calibration of redox thresholds in sedimentary systems. *Geochimica et Cosmochimica Acta*, *287*, 8–26.

Algeo, T.J. & Liu, J.S. (2020) A re-assessment of elemental proxies for paleoredox analysis. *Chemical Geology*, *540*.

Algeo, T.J. & Lyons, T.W. (2006) Mo-total organic carbon covariation in modern anoxic marine environments: implications for analysis of paleoredox and paleohydrographic conditions. *Paleoceanography*, *21*.

Algeo, T.J. & Maynard, J.B. (2004) Trace-element behavior and redox facies in core shales of Upper Pennsylvanian Kansas-type cyclothems. *Chemical Geology*, *206*, 289–318.

Algeo, T.J. & Maynard, J.B. (2008) Trace-metal covariation as a guide to water-mass conditions in ancient anoxic marine environments. *Geosphere*, *4*, 872–887.

Algeo, T.J. & Rowe, H. (2012) Paleoceanographic applications of trace-metal concentration data. *Chemical Geology*, *324*, 6–18.

Algeo, T.J. & Tribovillard, N. (2009) Environmental analysis of paleoceanographic systems based on molybdenum-uranium covariation. *Chemical Geology*, *268*, 211–225.

Anaconda. (2020) Anaconda software distribution version 2020.11. Computer software. Available from: https://anaconda.com/

Anell, I., Braathen, A., Olaussen, S. & Osmundsen, P.T. (2013) Evidence of faulting contradicts a quiescent northern Barents Shelf during the Triassic. *First Break*, *31*, 67–76.

Anell, I., Faleide, J.-I. & Braathen, A. (2016) Regional tectonosedimentary development of the highs and basins of the northwestern Barents Shelf. *Norwegian Journal of Geology*, *96*, 27–41.

Ardakani, O.H., Chappaz, A., Sanei, H. & Mayer, B. (2016) Effect of thermal maturity on remobilization of molybdenum in black shales. *Earth and Planetary Science Letters*, *449*, 311–320.

Atar, E., Marz, C., Schnetger, B., Wagner, T. & Aplin, A. (2019) Local to global controls on the deposition of organic-rich muds across the Late Jurassic Laurasian Seaway. *Journal of the Geological Society*, *176*, 1143–1153.

Bernhardsen, S. (2019) A sedimentological study of the organic-rich Botneheia Formation (Middle Triassic) with emphasis on the ichnogenus Thalassinoides, Edgeøya, Svalbard. MSc thesis, Norwegian University of Science and Technology (NTNU), 142 pp.

Bjerager, M., Alsen, P., Hovikoski, J., Lindstrom, S., Pilgaard, A., Stemmerik, L. & Therkelsen, J. (2019) Triassic lithostratigraphy of the Wandel Sea Basin, North Greenland. *Bulletin of the Geological Society of Denmark*, *67*, 83–105.

Bjorøy, M., Hall, P.B., Ferriday, I.L. & Mørk, A. (2009) Triassic source rocks of the Barents Sea and Svalbard. In: *AAPG datapages search and discovery article #10219*. AAPG International Conference & Exhibition, Denver, CO, 23 pp.

Boës, X., Rydberg, J., Martinez-Cortizas, A., Bindler, R. & Renberg, I. (2011) Evaluation of conservative lithogenic elements (Ti, Zr, Al, and Rb) to study anthropogenic element enrichments in lake sediments. *Journal of Paleolimnology*, *46*, 75–87.

Bohacs, K.M., Grabowski, G.J., Carroll, A.R., Mankiewicz, P.J., Miskell-Gerhardt, K.J., Schwalbach, J.R., Wegner, M.B. & Simo, J.A. (2005) Production, destruction, and dilution—the many paths to source-rock development. In: *Deposition of organic-carbon-rich sediments: models, 82*. SEPM Society for Sedimentary Geology. pp. 61–101.

Borchers, S.L., Schnetger, B., Boning, P. & Brumsack, H.J. (2005) Geochemical signatures of the Namibian diatom belt: perennial upwelling and intermittent anoxia. *Geochemistry Geophysics Geosystems*, *6*.

Brekke, T., Krajewski, K.P. & Hubred, J.H. (2014) Organic geochemistry and petrography of thermally altered sections of the Middle Triassic Botneheia Formation on south-western Edgeøya, Svalbard. *Norwegian Petroleum Directorate Bulletin*, *11*, 111–128.

Bue, E.P. & Andresen, A. (2014) Constraining depositional models in the Barents Sea region using detrital zircon U-Pb data from Mesozoic sediments in Svalbard. *Sediment Provenance Studies in Hydrocarbon Exploration and Production*, *386*, 261–279.

Calvert, S.E. & Pedersen, T.F. (2007) Elemental proxies for palaeoclimatic and palaeoceanographic variability in marine sediments: interpretation and application. In: C. Hillaire-Marcel and A. De Vernal (Eds.) *Proxies in late cenozoic paleoceanography*, vol. 1, pp. 567–644. Elsevier. Available from: https://www.sciencedirect.com/science/article/pii/S1572548007010196#aep-abstract-id28

Chen, J.B., Zhao, L.S., Algeo, T.J., Zhou, L., Zhang, L. & Qiu, H. (2019) Evaluation of paleomarine redox conditions using Mo-isotope data in low-[Mo] sediments: a case study from the Lower Triassic of South China. *Palaeogeography, Palaeoclimatology, Palaeoecology*, *519*, 178–193.

Craigie, N.W. (2015) Applications of chemostratigraphy in Middle Jurassic unconventional reservoirs in eastern Saudi Arabia. *Geoarabia*, *20*, 79–110.

Craigie, N. (2018) *Principles of elemental chemostratigraphy*. Cham: Springer International Publishing.

Craigie, N.W., Breuer, P. & Khidir, A. (2016) Chemostratigraphy and biostratigraphy of Devonian, Carboniferous and Permian sediments encountered in eastern Saudi Arabia: an integrated approach to reservoir correlation. *Marine and Petroleum Geology*, *72*, 156–178.

Creaney, S. & Passey, Q.R. (1993) Recurring patterns of total organic carbon and source rock quality within a sequence stratigraphic framework. *AAPG Bulletin*, *77*, 386–401.

Dahlgren, S., Hanesand, T., Mills, N., Patience, R., Brekke, T. & Sinding-Larsen, R. (1998) Norwegian geochemical standard samples: Svalbard rock – 1 (NGS SR-1). Norwegian Geochemical Standards Newsletter, 1.

Dallmann, W.K. & Elvevold, S. (2015) Bedrock geology. In: Dallmann, W. (Ed.) *Geoscience atlas of Svalbard*. Tromsø: Norwegian Polar Institute.

Demaison, G.J. & Moore, G.T. (1980) Anoxic environments and oil source bed genesis. *AAPG Bulletin*, *64*, 1179–1209.

Eggimann, D.W., Manheim, F.T. & Betzer, P.R. (1980) Dissolution and analysis of amorphous silica in marine sediments. *Journal of Sedimentary Research*, *50*, 215–225.

Eide, C.H., Klausen, T.G., Katkov, D., Suslova, A.A. & Helland-Hansen, W. (2018) Linking an Early Triassic delta to antecedent topography: source-to-sink study of the southwestern Barents Sea margin. *GSA Bulletin*, *130*, 263–283.

Eisenberg, R.A. & Harris, P.M. (1995) Application of chemostratigraphy and multivariate statistical analysis to differentiating

bounding stratigraphic surfaces. In: Pausé, P.H. & Candelaria, M.P. (Eds.) *Carbonate facies and sequence stratigraphy: practical applications of carbonate models*. Permian Basin Section-SEPM Publication 95–36/Permian Basin Graduate Center Publication 5–95, pp. 83–102.

Ellis, D.V. & Singer, J.M. (2007) Gamma ray devices. In: Ellis, D.V. & Singer, J.M. (Eds.) *Well logging for earth scientists*. Netherlands, Dordrecht: Springer, pp. 267–288.

Embry, A.F. (1993) Crockerland — the northwest source area for the Sverdrup Basin, Canadian Arctic Islands. In: Vorren, T.O., Bergsager, E., Dahl-Stamnes, A., Holter, E., Johansen, Å., Lie, Å. & Lund, T.B. (Eds.) *Arctic geology and petroleum potential. NPF Special Publication*, pp. 205–216.

England, W.A. & Mackenzie, A.S. (1989) Some aspects of the organic geochemistry of petroleum fluids. *Geologische Rundschau*, *78*, 291–303.

Faleide, J.I., Gudlaugsson, S.T. & Jacquart, G. (1984) Evolution of the western Barents Sea. *Marine and Petroleum Geology*, *1*, 123–150.

Ferriday, T. & Montenari, M. (2016) Chemostratigraphy and chemofacies of source rock analogues. In: Montenari, M. (Ed.) *Stratigraphy & timescales*, vol. 1, pp. 123–255.

Filippelli, G.M. (2011) Phosphate rock formation and marine phosphorus geochemistry: the deep time perspective. *Chemosphere*, *84*, 759–766.

Fleming, E.J., Flowerdew, M.J., Smyth, H.R., Scott, R.A., Morton, A.C., Omma, J.E., Frei, D. & Whitehouse, M.J. (2016) Provenance of Triassic sandstones on the southwest Barents Shelf and the implication for sediment dispersal patterns in northwest Pangaea. *Marine and Petroleum Geology*, *78*, 516–535.

Francois, R. (1988) A study on the regulation of the concentrations of some trace-metals (Rb, Sr, Zn, Pb, Cu, V, Cr, Ni, Mn and Mo) in saanich inlet sediments, British-Columbia, Canada. *Marine Geology*, *83*, 285–308.

Gilmullina, A., Klausen, T.G., Paterson, N.W., Suslova, A. & Eide, C.H. (2021) Regional correlation and seismic stratigraphy of Triassic Strata in the Greater Barents Sea: implications for sediment transport in Arctic basins. *Basin Research*, *33*, 1546–1579.

Glørstad-Clark, E., Birkeland, E.P., Nystuen, J.P., Faleide, J.I. & Midtkandal, I. (2011) Triassic platform-margin deltas in the western Barents Sea. *Marine and Petroleum Geology*, *28*, 1294–1314.

Glørstad-Clark, E., Faleide, J.I., Lundschien, B.A. & Nystuen, J.P. (2010) Triassic seismic sequence stratigraphy and paleogeography of the western Barents Sea area. *Marine and Petroleum Geology*, *27*, 1448–1475.

Goldberg, E.D. & Arrhenius, G.O.S. (1958) Chemistry of Pacific pelagic sediments. *Geochimica et Cosmochimica Acta*, *13*, 153–212.

Grabowski, J., Stoykova, K., Wierzbowski, H. & Wójcik-Tabol, P. (2021) Upper Berriasian chemostratigraphy, clay minerals and calcareous nannofossils of the Barlya section (Western Balkan, Bulgaria): implications for palaeoclimate and productivity changes, and stratigraphic correlations across the Alpine Tethys. *Palaeogeography, Palaeoclimatology, Palaeoecology*, *567*, 110252.

Grasby, S.E., Beauchamp, B., Embry, A. & Sanei, H. (2013) Recurrent Early Triassic ocean anoxia. *Geology*, *41*, 175–178.

Grasby, S.E., Beauchamp, B. & Knies, J. (2016) Early Triassic productivity crises delayed recovery from world's worst mass extinction. *Geology*, *44*, 779–782.

Grasby, S.E., Knies, J., Beauchamp, B., Bond, D.P.G., Wignall, P. & Sun, Y.D. (2020) Global warming leads to Early Triassic nutrient stress across northern Pangea. *Geological Society of America Bulletin*, *132*, 943–954.

Hammer, Ø., Jones, M.T., Schneebeli-Hermann, E., Hansen, B.B. & Bucher, H. (2019) Are Early Triassic extinction events associated with mercury anomalies? A reassessment of the Smithian/Spathian boundary extinction. *Earth-Science Reviews*, *195*, 179–190.

Hansen, B.B., Hammer, O. & Nakrem, H.A. (2018) Stratigraphy and age of the Grippia niveau bonebed, Lower Triassic Vikinghøgda Formation, Spitsbergen. *Norwegian Journal of Geology*, *98*, 175–187.

Helz, G.R., Bura-Nakic, E., Mikac, N. & Ciglenecki, I. (2011) New model for molybdenum behavior in euxinic waters. *Chemical Geology*, *284*, 323–332.

Helz, G.R., Miller, C.V., Charnock, J.M., Mosselmans, J.F.W., Pattrick, R.A.D., Garner, C.D. & Vaughan, D.J. (1996) Mechanism of molybdenum removal from the sea and its concentration in black shales: EXAFS evidence. *Geochimica et Cosmochimica Acta*, *60*, 3631–3642.

Hildred, G. (2012) Shale resource plays in the Horn River Basin, British Columbia, Canada: using high resolution chemostratigraphy to determine well-bore pathways in multi-lateral drilling campaigns. *Houston Geological Society Bulletin*, *55*, 21 and 23.

Hildred, G., Ratcliffe, K. & Schmidt, K. (2011) Application of inorganic whole-rock geochemistry to shale resource plays: an example from the Eagle Ford Shale, Texas. *Houston Geological Society Bulletin*, *53*, 31–38.

Hounslow, M.W., Hu, M.Y., Mørk, A., Weitschat, W., Vigran, J.O., Karloukovski, V. & Orchard, M.J. (2008) Intercalibration of Boreal and Tethyan time scales: the magnetobiostratigraphy of the Middle Triassic and the latest Early Triassic from Spitsbergen, Arctic Norway. *Polar Research*, *27*, 469–490.

Hounslow, M.W., Peters, C., Mørk, A., Weitschat, W. & Vigran, J.O. (2008) Biomagnetostratigraphy of the Vikinghogda Formation, Svalbard (Arctic Norway), and the geomagnetic polarity timescale for the Lower Triassic. *Geological Society of America Bulletin*, *120*, 1305–1325.

Høy, T. & Lundschien, B.A. (2011) Triassic deltaic sequences in the northern Barents Sea. In: *Arctic Petroleum Geology* (Eds Spencer, A.M., Embry, A.F., Gautier, D.L., Stoupakova, A.V. & Sørensen, K.) vol. 35, pp. 249–260. The Geological Society of London.

Isaksen, G.H. & Bohacs, K.M. (1995) Geological controls of source rock geochemistry through relative sea level; Triassic, Barents Sea. In: Katz, B.J. (Ed.) *Petroleum source rocks*. Berlin, Heidelberg: Springer, pp. 25–50.

Jarvis, I., Burnett, W.C., Nathan, Y., Almbaydin, F.S.M., Attia, A.K.M., Castro, L.N., Flicoteaux, R., Hilmy, M.E., Husain, V., Qutawnah, A.A., Serjani, A. & Zanin, Y.N. (1994) Phosphorite geochemistry – state-of-the-art and environmental concerns. *Eclogae Geologicae Helvetiae*, *87*, 643–700.

Jones, B. & Manning, D.A.C. (1994) Comparison of Geochemical indexes used for the interpretation of palaeoredox conditions in ancient mudstones. *Chemical Geology*, *111*, 111–129.

Katz, B.J. (2005) Controlling factors on source rock development—a review of productivity, preservation, and sedimentation rate. In: *The deposition of organic-carbon-rich sediments: models, mechanisms, and consequences. SEPM Special Publication*, *82*, pp. 7–16. SEPM Society for Sedimentary Geology.

Klausen, T.G., Nyberg, B. & Helland-Hansen, W. (2019) The largest delta plain in Earth's history. *Geology*, *47*, 470–474.

Klausen, T.G., Ryseth, A.E., Helland-Hansen, W., Gawthorpe, R. & Laursen, I. (2015) Regional development and sequence stratigraphy of the Middle to Late Triassic Snadd Formation, Norwegian Barents Sea. *Marine and Petroleum Geology*, *62*, 102–122.

Kolodny, Y. (2009) Phosphorite. In: Gornitz, V. (Ed.) *Encyclopedia of paleoclimatology and ancient environments*. Dordrecht: Springer, pp. 775–780.

Krajewski, K.P. (2008) The Botneheia Formation (Middle Triassic) in Edgeøya and Barentsøya, Svalbard: lithostratigraphy, facies, phosphogenesis, paleoenvironment. *Polish Polar Research*, *29*, 319–364.

Krajewski, K.P. (2013) Organic matter-apatite-pyrite relationships in the Botneheia Formation (Middle Triassic) of eastern Svalbard: relevance to the formation of petroleum source rocks in the NW Barents Sea shelf. *Marine and Petroleum Geology*, *45*, 69–105.

Krajewski, K.P. & Weitschat, W. (2015) Depositional History of the Youngest Strata of the Sassendalen Group (Bravaisberget Formation, Middle Triassic-Carnian) in Southern Spitsbergen, Svalbard. *Annales Societatis Geologorum Poloniae*, *85*, 151–175.

LaGrange, M.T., Konhauser, K.O., Catuneanu, O., Harris, B.S., Playter, T.L. & Gingras, M.K. (2020) Sequence stratigraphy in organic-rich marine mudstone successions using chemostratigraphic datasets. *Earth-Science Reviews*, *203*, 103137.

Leith, T.L., Weiss, H.M., Mørk, A., Århus, N., Elvebakk, G., Embry, A.F., Brooks, P.W., Stewart, K.R., Pchelina, T.M., Bro, E.G., Verba, M.L., Danyushevskaya, A. & Borisov, A.V. (1993) Mesozoic hydrocarbon source rocks of the Arctic region. In: Vorren, T.O., Bergsager, E., Dahl-Stamnes, A., Holter, E., Johansen, Å., Lie, Å. & Lund, T.B. (Eds.), *Arctic geology and petroleum potential*. *NPF Special Publication*, pp. 1–25. Amsterdam: Elsevier.

Lerch, B., Karlsen, D.A., Abay, T.B., Duggan, D., Seland, R. & Backer-Owe, K. (2016a) Regional petroleum alteration trends in Barents Sea oils and condensates as a clue to migration regimes and processes. *AAPG Bulletin*, *100*, 165–190.

Lerch, B., Karlsen, D.A., Matapour, Z., Seland, R. & Backer-Owe, K. (2016b) Organic geochemistry of Barents Sea petroleum: thermal maturity and alteration and mixing processes in oils and condensates. *Journal of Petroleum Geology*, *39*, 125–148.

Lerch, B., Karlsen, D.A., Seland, R. & Backer-Owe, K. (2017) Depositional environment and age determination of oils and condensates from the Barents Sea. *Petroleum Geoscience*, *23*, 190–209.

Lerch, B., Karlsen, D.A., Thiessen, O., Abay, T.B., van Soelen, E.E., Kurschner, W.M., Planke, S. & Backer-Owe, K. (2018) Investigations on the use of triaromatic dimethylcholesteroids as age-specific biomarkers in bitumens and oils from Arctic Norway. *Organic Geochemistry*, *122*, 1–16.

Lewan, M.D. (1984) Factors controlling the proportionality of vanadium to nickel in crude oils. *Geochimica et Cosmochimica Acta*, *48*, 2231–2238.

Liang, L.J., Sun, Y.B., Beets, C.J., Prins, M.A., Wu, F. & Vandenberghe, J. (2013) Impacts of grain size sorting and chemical weathering on the geochemistry of Jingyuan loess in the northwestern Chinese Loess Plateau. *Journal of Asian Earth Sciences*, *69*, 177–184.

Line, L.H., Jahren, J. & Hellevang, H. (2018) Mechanical compaction in chlorite-coated sandstone reservoirs – examples from Middle – Late Triassic channels in the southwestern Barents Sea. *Marine and Petroleum Geology*, *96*, 348–370.

Lord, G.S., Johansen, S.K., Stoen, S.J. & Mørk, A. (2017) Facies development of the Upper Triassic succession on Barentsøya, Wilhelmøya and NE Spitsbergen, Svalbard. *Norwegian Journal of Geology*, *97*, 33–62.

Lundschien, B.A., Høy, T. & Mørk, A. (2014) Triassic hydrocarbon potential in the Northern Barents Sea: integrating Svalbard and stratigraphic core data. *Norwegian Petroleum Directorate Bulletin*, *11*, 3–20.

Lutz, R., Klitzke, P., Weniger, P., Blumenberg, M., Franke, D., Reinhardt, L., Ehrhardt, A. & Berglar, K. (2021) Basin and petroleum systems modelling in the northern Norwegian Barents Sea. *Marine and Petroleum Geology*, *130*, 105128.

Magoon, L.B. & Dow, W.G. (1994) The Petroleum System. In: Magoon, L.B. & Dow, W.G. (Eds.) *The petroleum system – from source to trap*, pp. 3–24. AAPG.

Mansour, A., Gentzis, T., Carvajal-Ortiz, H., Tahoun, S.S., Elewa, A.M.T. & Mohamed, O. (2020) Source rock evaluation of the Cenomanian Raha Formation, Bakr oil field, Gulf of Suez, Egypt: observations from palynofacies, RGB-based sporomorph microscopy, and organic geochemistry. *Marine and Petroleum Geology*, *122*, 104661.

Mongenot, T., Tribovillard, N.-P., Desprairies, A., Lallier-Vergès, E. & Laggoun-Defarge, F. (1996) Trace elements as palaeoenvironmental markers in strongly mature hydrocarbon source rocks: the Cretaceous La Luna Formation of Venezuela. *Sedimentary Geology*, *103*, 23–37.

Morford, J.L. & Emerson, S. (1999) The geochemistry of redox sensitive trace metals in sediments. *Geochimica et Cosmochimica Acta*, *63*, 1735–1750.

Mørk, A. & Bjorøy, M. (1984) Mesozoic source rocks on Svalbard. In: Spencer, A.M. (Ed.) *Proceedings of the North European Margin Symposium (NEMS '83)*, organized by the Norwegian Petroleum Society and held at the Norwegian Institute of Technology (NTH) in Trondheim 9–11 May (Ed), Petroleum Geology of the North European Margin, pp. 371–382. Springer Netherlands.

Mørk, A. & Bromley, R.G. (2008) Ichnology of a marine regressive systems tract: the Middle Triassic of Svalbard. *Polar Research*, *27*, 339–359.

Mørk, A., Egorov, A.Y. & Embry, A.F. (1994) Base Olenekian and base Anisian sequence boundaries produced by Triassic circumpolar 'synchronous' transgressions. In: Thurston, D.K. & Fujita, K. (Eds.) *International Conference on Arctic Margins 1992 Proceedings*. OCS Study MMS 940040. Mineral Management Service, Alaska OCR Region: US. Department of the Interior, pp. 9–14.

Mørk, A. & Elvebakk, G. (1999) Lithological description of subcropping Lower and Middle Triassic rocks from the Svalis Dome, Barents Sea. *Polar Research*, *18*, 83–104.

Mørk, A., Elvebakk, G., Forsberg, A.W., Hounslow, M.W., Nakrem, H.A., Vigran, J.O. & Weitschat, W. (1999) The type section of the Vikinghøgda Formation: a new Lower Triassic unit in central and eastern Svalbard. *Polar Research*, *18*, 51–82.

Mørk, A., Embry, A. & Weitschat, W. (1989) Triassic transgressive-regressive cycles in the Sverdrup Basin, Svalbard and the Barents Shelf. In: Collinson, J. (Ed.) *Correlation in Hydrocarbon Exploration*. Graham and Trotman: Bergen, Norway, pp. 113–130.

Mørk, A., Knarud, R. & Worsley, D. (1982) Depositional and diagenetic environments of the Triassic and Lower Jurassic succession of Svalbard. In: Embry, A.F. & Balkwill, H.R. (Eds.) *Arctic geology and geophysics: Proceedings of the Third International Symposium on Arctic Geology*, *Canadian Society of Petroleum Geologists Memoir*, *8*, pp. 371–398.

Mueller, S., Veld, H., Nagy, J. & Kürschner, W.M. (2014) Depositional history of the Upper Triassic Kapp Toscana Group on Svalbard, Norway, inferred from palynofacies analysis and organic geochemistry. *Sedimentary Geology*, *310*, 16–29.

Muller, R., Klausen, T.G., Faleide, J.I., Olaussen, S., Eide, C.H. & Suslova, A. (2019) Linking regional unconformities in the Barents Sea to compression-induced forebulge uplift at the Triassic-Jurassic transition. *Tectonophysics*, *765*, 35–51.

Niebuhr, B. (2005) Geochemistry and time-series analyses of orbitally forced Upper Cretaceous marl–limestone rhythmites (Lehrte West Syncline, northern Germany). *Geological Magazine*, *142*, 31–55.

Norwegian Petroleum Directorate (2017) Geological assessment of petroleum resources in eastern parts of Barents Sea North. Norwegian Petroleum Directorate.

Ogata, K., Mulrooney, M.J., Braathen, A., Maher, H., Osmundsen, P.T., Anell, I., Smyrak-Sikora, A.A. & Balsamo, F. (2018) Architecture, deformation style and petrophysical properties of growth fault systems: the Late Triassic deltaic succession of southern Edgeøya (East Svalbard). *Basin Research*, *30*, 1042–1073.

Pang, H.L., Pan, B.T., Garzanti, E., Gao, H.S., Zhao, X. & Chen, D.B. (2018) Mineralogy and geochemistry of modern Yellow River sediments: implications for weathering and provenance. *Chemical Geology*, *488*, 76–86.

Parrish, J.T. & Curtis, R.L. (1982) Atmospheric circulation, upwelling, and organic-rich rocks in the Mesozoic and Cenozoic Eras. *Palaeogeography Palaeoclimatology Palaeoecology*, *40*, 31–66.

Parrish, J.T., Droser, M.L. & Bottjer, D.J. (2001) A Triassic upwelling zone: the Shublik Formation, Arctic Alaska, USA. *Journal of Sedimentary Research*, *71*, 272–285.

Paterson, N.W., Mangerud, G., Cetean, C.G., Mørk, A., Lord, G.S., Klausen, T.G. & Mørkved, P.T. (2016) A multidisciplinary biofacies characterisation of the Late Triassic (late Carnian–Rhaetian) Kapp Toscana Group on Hopen, Arctic Norway. *Palaeogeography, Palaeoclimatology, Palaeoecology*, *464*, 16–42.

Paterson, N.W., Mangerud, G. & Mørk, A. (2017) Late Triassic (early Carnian) palynology of shallow stratigraphical core 7830/5-U-1, offshore Kong Karls Land, Norwegian Arctic. *Palynology*, *41*, 230–254.

Pčelina, T.M. & Korčinskaja, M.V. (2008) Palaeogeographic reconstructions of the Russian Boreal areas and Svalbard during the Triassic. *Polar Research*, *27*, 491–494.

Pedersen, J.H., Hammer, E., Bernhardsen, S., Engelschiøn, V.S., Hansen, B.B., Hurum, J.H., Hammer, Ø., Hansen, G. & Nyjordet, B. (2020) Verdens første oljeboring på fossil blekksprut!. In: Nakrem, H.A. (Ed.) *NGF Oslo meetings Autumn 2020*. Olso, Norway: Norsk Geologisk Forening.

Pedersen, T.F. & Calvert, S.E. (1990) Anoxia vs productivity – what controls the formation of organic-carbon-rich sediments and sedimentary-rocks? *AAPG Bulletin*, *74*, 454–466.

Percy, E.L. & Pedersen, P.K. (2020) Detailed facies analysis of Cenomanian-Turonian organic-rich mudstones: implications for depositional controls on source rocks. *The Depositional Record*, *6*, 409–430.

Potter, P.E., Maynard, J.B. & Depetris, P.J. (2005) *Mud and mudstones*. Berlin Heidelberg: Springer-Verlag.

Qin, Z.Y., Yang, X. & Jiang, M.M. (1985) Chemostratigraphic correlation of the Middle and Upper Proterozoic between the Yanshan and Shennongjia Basins. *Precambrian Research*, *29*, 77–91.

Raiswell, R., Buckley, F., Berner, R.A. & Anderson, T.F. (1988) Degree of pyritization of iron as a paleoenvironmental Indicator of bottom-water oxygenation. *Journal of Sedimentary Petrology*, *58*, 812–819.

Ramirez-Montoya, E., Madhavaraju, J. & Monreal, R. (2021) Geochemistry of the sedimentary rocks from the Antimonio and Río Asunción formations, Sonora, Mexico: implications for weathering, provenance and chemostratigraphy. *Journal of South American Earth Sciences*, *106*, 103035.

Riboulleau, A., Baudin, F., Deconinck, J.F., Derenne, S., Largeau, C. & Tribovillard, N. (2003) Depositional conditions and organic matter preservation pathways in an epicontinental environment: the Upper Jurassic Kashpir Oil Shales (Volga Basin, Russia). *Palaeogeography, Palaeoclimatology, Palaeoecology*, *197*, 171–197.

Riis, F., Lundschien, B.A., Høy, T., Mørk, A. & Mørk, M.B.E. (2008) Evolution of the Triassic shelf in the northern Barents Sea region. *Polar Research*, *27*, 318–338.

Rohatgi, A. (2020) Webplotdigitizer version 4.4. Computer software. Available from: https://automeris.io/WebPlotDigitizer

Rosenberg, Y.O., Reznik, I.J., Vinegar, H.J., Feinstein, S. & Bartov, Y. (2021) Comparing natural and artificial thermal maturation of a Type II-S source rock, Late Cretaceous, Israel. *Marine and Petroleum Geology*, *124*, 104773.

Rothwell, R.G. & Croudace, I.W. (2015) Twenty years of XRF core scanning marine sediments: what do geochemical proxies tell us? In: Croudace, I.W. & Rothwell, R.G. (Eds.) *Micro-XRF studies of sediment cores: applications of a non-destructive tool for the environmental sciences, Developments in Paleoenvironmental Research*. Dordrecht: Springer Netherlands, pp. 25-102

Sanei, H., Ardakani, O.H., Akai, T., Akihisa, K., Jiang, C.Q. & Wood, J.M. (2020) Core versus cuttings samples for geochemical and petrophysical analysis of unconventional reservoir rocks. *Scientific Reports*, *10*.

Schatz, W. (2005) Palaeoecology of the Triassic black shale bivalve Daonella—new insights into an old controversy. *Palaeogeography, Palaeoclimatology, Palaeoecology*, *216*, 189–201.

Schoepfer, S.D., Shen, J., Wei, H., Tyson, R.V., Ingall, E. & Algeo, T.J. (2015) Total organic carbon, organic phosphorus, and biogenic barium fluxes as proxies for paleomarine productivity. *Earth-Science Reviews*, *149*, 23–52.

Schou, L., Mørk, A. & Bjorøy, M. (1984) Correlation of source rocks and migrated hydrocarbons by GC-MS in the Middle Triassic of Svalbard. *Organic Geochemistry*, *6*, 513–520.

Scott, C. & Lyons, T.W. (2012) Contrasting molybdenum cycling and isotopic properties in euxinic versus non-euxinic sediments and sedimentary rocks: refining the paleoproxies. *Chemical Geology*, *324*, 19–27.

Silva, R.L., Carlisle, C.A.M. & Wach, G. (2017) A new TOC, Rock-Eval, and carbon isotope record of Lower Jurassic source rocks from the Slyne Basin, offshore Ireland. *Marine and Petroleum Geology*, *86*, 499–511.

Smelror, M. & Sollid, K. (2007) Blekkspruter Fulle Av Olje. *GEO*, *2*, 28–29.

Sømme, T.O., Dore, A.G., Lundin, E.R. & Torudbakken, B.O. (2018) Triassic-Paleogene paleogeography of the Arctic: implications for sediment routing and basin fill. *AAPG Bulletin*, *102*, 2481–2517.

Song, J., Littke, R., Maquil, R. & Weniger, P. (2014) Organic facies variability in the Posidonia Black Shale from Luxembourg: implications for thermal maturation and depositional environment. *Palaeogeography, Palaeoclimatology, Palaeoecology*, *410*, 316–336.

Steel, R.J. & Worsley, D. (1984) Svalbard's post-Caledonian strata — an atlas of sedimentational patterns and palaeogeographic evolution. In: Spencer, A.M. (Ed.) *Petroleum geology of the North European margin*. Graham and Trotman, pp. 209-135.

Sun, Y., Joachimski, M.M., Wignall, P.B., Yan, C., Chen, Y., Jiang, H., Wang, L. & Lai, X. (2012) Lethally hot temperatures during the Early Triassic greenhouse. *Science*, *338*, 366–370.

Taylor, K.G. & Macquaker, J.H.S. (2014) Diagenetic alterations in a silt- and clay-rich mudstone succession: an example from the Upper Cretaceous Mancos Shale of Utah, USA. *Clay Minerals*, *49*, 213–227.

Taylor, S.R. & McLennan, S.M. (1985) *The continental crust: its composition and evolution*. London: Blackwell, 312 pp.

Thöle, H., Bornemann, A., Heimhofer, U., Luppold, F.W., Blumenberg, M., Dohrmann, R. & Erbacher, J. (2019) Using high-resolution XRF analyses as a sequence stratigraphic tool in a mudstone-dominated succession (Early Cretaceous, Lower Saxony Basin, Northern Germany). *The Depositional Record*, *6*, 236–258.

Tissot, B.P. & Welte, D.H. (1984) Geological control of petroleum type. In: *Petroleum formation and occurrence*, 2nd edition, pp. 699. Berlin, Germany: Springer-Verlag.

Tribovillard, N., Algeo, T.J., Baudin, F. & Riboulleau, A. (2012) Analysis of marine environmental conditions based on molybdenum–uranium covariation—applications to Mesozoic paleoceanography. *Chemical Geology*, *324–325*, 46–58.

Tribovillard, N., Algeo, T.J., Lyons, T. & Riboulleau, A. (2006) Trace metals as paleoredox and paleoproductivity proxies: an update. *Chemical Geology*, *232*, 12–32.

Tyson, R.V. (1995) *Sedimentary organic matter*. Dordrecht: Springer.

Van der Weijden, C.H. (2002) Pitfalls of normalization of marine geochemical data using a common divisor. *Marine Geology*, *184*, 167–187.

Vigran, J.O., Mangerud, G., Mørk, A., Bugge, T. & Weitschat, W. (1998) Biostratigraphy and sequence stratigraphy of the Lower and Middle Triassic deposits from the Svalis Dome, Central Barents Sea, Norway. *Palynology*, *22*, 89–141.

Vigran, J.O., Mangerud, G., Mørk, A., Worsley, D. & Hochuli, P.A. (2014) Palynology and geology of the Triassic succession of Svalbard and the Barents Sea. Norwegian Geological Survey.

Vigran, J.O., Mørk, A., Forsberg, A.W., Weiss, H.M. & Weitschat, W. (2008) Tasmanites algae-contributors to the Middle Triassic hydrocarbon source rocks of Svalbard and the Barents Shelf. *Polar Research*, *27*, 360–371.

Wedepohl, K.H. (2004) The composition of Earth's upper crust, natural cycles of elements, natural resources. In: Merian, E., Anke, M., Ihnat, M. & Stoeppler, M. (Eds.) *Elements and their compounds in the environment*, 2nd edition. Weinheim: WILEY-VCH Verlag GmbH & Co. KGaA, pp. 3–16.

Weitschat, W. & Lehmann, U. (1983) Stratigraphy and ammonoids from the Middle Triassic Botneheia Formation (Daonella Shales) of Spitsbergen. *Mitteilungen Geologisch—paläontologisches Institut Der Universität Hamburg*, *54*, 27–54.

Wesenlund, F., Grundvåg, S.-A., Engelschiøn, V.S., Thießen, O. & Pedersen, J.H. (2021) Linking facies variations, organic carbon richness and bulk bitumen content – a case study of the organic-rich Middle Triassic shales from eastern Svalbard. *Marine and Petroleum Geology*, *132*, 105168.

Wignall, P.B., Bond, D.P.G., Sun, Y.D., Grasby, S.E., Beauchamp, B., Joachimski, M.M. & Blomeier, D.P.G. (2016) Ultra-shallow-marine anoxia in an Early Triassic shallow-marine clastic ramp (Spitsbergen) and the suppression of benthic radiation. *Geological Magazine*, *153*, 316–331.

Wright, A.M., Spain, D. & Ratcliffe, K.T. (2010) Application of inorganic whole rock geochemistry to shale resource plays. In: *Canadian Unconventional Resources & International Petroleum Conference*. Calgary, AB, Canada: Society of Petroleum Engineers.

Xu, G.P., Hannah, J.L., Bingen, B., Georgiev, S. & Stein, H.J. (2012) Digestion methods for trace element measurements in shales: paleoredox proxies examined. *Chemical Geology*, *324*, 132–147.

Xu, G., Hannah, J.L., Stein, H.J., Mørk, A., Vigran, J.O., Bingen, B., Schutt, D.L. & Lundschien, B.A. (2014) Cause of Upper Triassic climate crisis revealed by Re–Os geochemistry of Boreal black shales. *Palaeogeography, Palaeoclimatology, Palaeoecology*, *395*, 222–232.

Zhang, F.F., Romaniello, S.J., Algeo, T.J., Lau, K.V., Clapham, M.E., Richoz, S., Herrmann, A.D., Smith, H., Horacek, M. & Anbar, A.D. (2018) Multiple episodes of extensive marine anoxia linked to global warming and continental weathering following the latest Permian mass extinction. *Science Advances*, *4*, e1602921. Available from: https://doi.org/10.1126/sciadv.1602921

Zhang, J., Zeng, Y. & Slatt, R. (2019) XRF (X-ray fluorescence) applied to characterization of unconventional Woodford Shale (Devonian, U.S.A.) lateral well heterogeneity. *Fuel*, *254*.

Zhao, J., Jin, Z., Jin, Z., Geng, Y., Wen, X. & Yan, C. (2016) Applying sedimentary geochemical proxies for paleoenvironment interpretation of organic-rich shale deposition in the Sichuan Basin, China. *International Journal of Coal Geology*, *163*, 52–71.

Zuchuat, V., Sleveland, A.R.N., Twitchett, R.J., Svensen, H.H., Turner, H., Augland, L.E., Jones, M.T., Hammer, O., Hauksson, B.T., Haflidason, H., Midtkandal, I. & Planke, S. (2020) A new high-resolution stratigraphic and palaeoenvironmental record spanning the End-Permian Mass Extinction and its aftermath in central Spitsbergen, Svalbard. *Palaeogeography, Palaeoclimatology, Palaeoecology*, *554*, 109732.

SUPPORTING INFORMATION

Additional supporting information may be found in the online version of the article at the publisher's website.

How to cite this article: Wesenlund, F., Grundvåg, S.-A., Engelschiøn, V.S., Thießen, O. & Pedersen, J.H. (2022) Multi-elemental chemostratigraphy of Triassic mudstones in eastern Svalbard: Implications for source rock formation in front of the World's largest delta plain. *The Depositional Record*, 00, 1–36. Available from: https://doi.org/10.1002/dep2.182